

JPRS-CST-90-020

6 AUGUST 1990



**FOREIGN  
BROADCAST  
INFORMATION  
SERVICE**

**DISTRIBUTION STATEMENT A**  
Approved for public release;  
Distribution Unlimited

# ***JPRS Report***

# **Science & Technology**

***China***

GALLIUM ARSENIDE LASER DIODES

19980506 060

REPRODUCED BY  
U.S. DEPARTMENT OF COMMERCE  
NATIONAL TECHNICAL INFORMATION SERVICE  
SPRINGFIELD, VA. 22161

**DTIC QUALITY INSPECTED 3**

JPRS-CST-90-020

6 AUGUST 1990

## SCIENCE & TECHNOLOGY

### CHINA

#### GALLIUM ARSENIDE LASER DIODES

90FE0052 Beijing BANDAOTI XUEBAO [CHINESE JOURNAL OF SEMICONDUCTORS] in Chinese Vol 10 No 12, Dec 89; Vol 11 No 1, Jan 90; Vol 11 No 2, Feb 90; Vol 11 No 3, Mar 90; Vol 11 No 4, Apr 90; Vol 11 No 5, May 90

#### Contents

Thermal Annealing in MBE-Grown High-Purity Thin Films [Xu Hongda, T.G. Anderson].....	1
GaAlAs/GaAs SQW SCH Laser Diode Fabricated by MOCVD [Zhuang Wanru, Shi Zhiwen, et al.].....	6
RTA of Si and As Dual Implantation Into GaAs [Zhu Dehua, Li Guohui, et al.].....	12
In-Situ Monitoring of High-Quality Diffraction Gratings [Xie Jianping, Ming Hai, et al.].....	17
Hybrid Parabolic-Reflector 2D Surface-Emitting Visible Laser Diode [Zhang Xiaobo, Du Guotong, et al.].....	24
Characteristics of GaAs/GaAlAs CCTS Bistable Laser [Wang Qiming, Wu Ronghan, et al.].....	29
Single-Lobe Phase-Locked TCSIS Semiconductor Laser Array [Zhao Fanghai, Du Guotong, et al.].....	36
GaAs/GaAlAs SQW Electroabsorption and Light Modulation [Zhu Longde, Xiong Feike, et al.].....	40

Bistable Laser Diode Integrated Monolithically With Photodetector [Yan Xuguang].....	50
Integrated Devices With Optical Dielectric Layers and MQW's [Lin Shiming].....	56
Visible Terraced Substrate Inner Stripe Semiconductor Laser [Du Guotong, Zhang Xiaobo, et al.].....	64
Monolithic Integration of Amplifier With MSM-PD on GaAs [Yang Qinqing, Gao Junhua].....	71

## Thermal Annealing in MBE-Grown High-Purity Thin Films

90FE0052A Beijing BANDAOTI XUEBAO [CHINESE JOURNAL OF SEMICONDUCTORS] in Chinese Vol 10 No 12, Dec 89 (MS Received 8 Nov 88) pp 912-916

[Article by Xu Hongda [1776 7703 6671] of the Institute of Semiconductors, Chinese Academy of Sciences (CAS), and T. G. Anderson of the Department of Physics, Chalmers University of Technology, Sweden: "Effect of Thermal Annealing on Deep Levels in High-Purity MBE-Grown GaAs Thin Films"; the work was completed at the Chalmers University of Technology in Sweden and presented at the Sixth Chinese National Semiconductor Physics Conference]

### [Text] Abstract

Deep-level transient spectroscopy (DLTS) is used to study the deep levels in high-purity GaAs thin films grown by molecular beam epitaxy (MBE). High-purity GaAs films with gold electrodes are annealed at different temperatures and both the position and shape of the corresponding DLTS peaks changes. This is due to the reaction between the gold electrode and the GaAs thin film during annealing, resulting in a variety of DLTS peaks. After removal of the reactant by using the mesa-etching technique of device fabrication, the DLTS peak is reduced to a single peak. In this work, I-V [current voltage] characteristics are also measured in order to analyze and discuss the changes in the DLTS peaks.

Key Words: molecular beam epitaxy, GaAs thin films, deep level, thermal annealing.

### I. Introduction

Electrical characteristics of a semiconductor are usually measured through metallic electrodes. Many useful properties are produced as a result of making such contacts. Especially in thin-layer GaAs, the fabrication of its contact interface is a critical step in making such devices as the MESFET (metal-semiconductor field effect transistor), HEMT (high electron mobility transistor), Schottky diode, and IMPATT (impact avalanche and transit time) diode. In general, the semiconductor contact interface can be divided into two categories: reactive and nonreactive. The former is frequently seen in the making of semiconductor devices. Almost all metallic contacts in GaAs devices



involve reactions with GaAs to various degree. The interface between gold and GaAs has been an interesting research subject and a number of studies have already been conducted.<sup>1-3</sup> In order to obtain some understanding on the basic properties of the deep energy levels of high-purity GaAs thin films, Au [gold] Schottky diodes were made from high-purity MBE-grown GaAs thin films to study the effect of thermal annealing on the DLTS spectrum. This type of study has heretofore not appeared in the literature.

## II. Experimental

### 1. Specimen Preparation

The GaAs specimens were grown on a (001) Si-doped GaAs substrate using a Varian MBE-360 molecular beam epitaxy system. The substrate temperature was held at 625°C and the growth rate of 1  $\mu\text{m}/\text{hour}$  was maintained by regulating the  $\text{As}_4/\text{Ga}$  beam ratio to 5:1. The beams were measured by ion gauges placed next to the substrate. The steady growth of As provided a (2x4) surface structure.

The structural process for the GaAs specimens includes growing a 0.5- $\mu\text{m}$  thick Si-doped buffer layer ( $n = 2 \times 10^{18}\text{cm}^{-3}$ ) on the substrate and then growing a 2.5- $\mu\text{m}$  thick high-purity GaAs layer ( $n = 8 \times 10^{14}\text{cm}^{-3}$ ). After the crystal was grown, the substrate temperature was lowered to approximately 100°C and a 0.5-mm diameter, 1500 Å-thick gold Schottky contact was formed on top of the specimen. The indium on the back side of the substrate (which was used to stick the substrate to the holder during MBE) is used as the ohmic contact. A diamond cutter was used to cut the gold-plated GaAs wafer into chips to be placed in the copper seat of a TO-5 package for testing. A 50- $\mu\text{m}$  diameter aluminum wire was ultrasonically welded onto the gold contact and the package.

### 2. Measurement

The DLTS unit (manufactured by INNOVANCE in Sweden) includes its central components, a heating circuit, a low-temperature specimen holder with analog temperature signal output, an improved capacitance meter, a pulse generator, an oscilloscope, and an X-Y recorder. In order to ensure that measurements were made under low-field conditions, the series resistance of the specimens was checked so that it did not affect the capacitance signal. The DLTS spectra of the specimens, before and after annealing, were measured by maintaining the same pulse bias, rate window, amplification gain, and X-Y recorder settings.

Prior to annealing, the current-voltage characteristics of the diodes were measured first and their DLTS spectra were measured immediately afterward. diodes were annealed in an  $\text{N}_2 + 3\%\text{H}_2$  atmosphere at 200, 275, 330, 380, and 430°C for 5 and 7 minutes. After each annealing process, the current-voltage characteristics and DLTS were measured.

## III. Experimental Results and Discussion

The DLTS spectra of the same diode annealed in the nitrogen/hydrogen mixture at various temperatures are shown in Figure 1. For ease of description, the three DLTS peaks measured prior to annealing are labeled as A (0.07 eV,

$\sigma_{\infty} = 2.25 \times 10^{-19} \text{ cm}^2$ ), B (0.59 eV,  $\sigma_{\infty} = 1.41 \times 10^{-13} \text{ cm}^2$ ), and C (0.63 eV,  $\sigma_{\infty} = 8.72 \times 10^{-12} \text{ cm}^2$ ). They are equivalent to  $M_0$ ,  $M_5$ , and  $M_6$  measured by D.V. Lang.<sup>4</sup> After annealing at 200°C, peaks A and C essentially did not change and peak B disappeared. After annealing at 275°C, peak A almost disappeared and peak C shifted slightly toward a lower temperature. In addition, two new peaks, D (0.46 eV) and E (0.69 eV), emerged on either side. After annealing at 330°C, peak C returned to its original position, peak E dropped down and peak D became more distinct. After annealing at 380°C, the DLTS plot essentially returned to its original shape. After annealing at 430°C, large amplitude oscillation was found in the low-temperature region and a new peak F (0.26 eV) was observed. At this time, peak D obviously had shifted toward a lower H. This apparent shift of the DLTS peaks after annealing at 200, 275, and 330°C might be due to the fact that thermal treatment in this temperature region could easily form  $\beta$ -phase Au-Ga and  $\text{Au}_3\text{Ga}_2$ .<sup>5</sup> The DLTS peaks that emerged after annealing at 430°C might be due to the orderless atomic arrangement at the interface.<sup>6</sup>

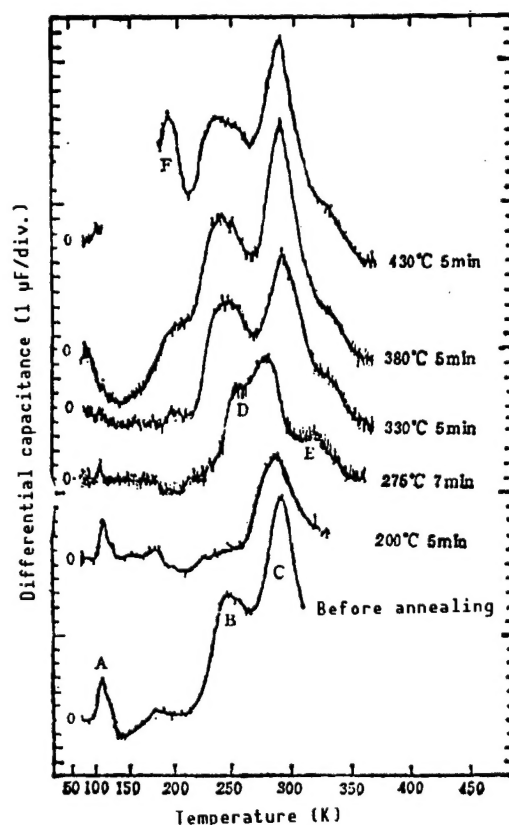


Figure 1. DLTS Spectra After Annealing at Various Temperatures at  $\text{N}_2 + 3\% \text{H}_2$

Figure 2 shows the overall deep-energy-level concentration as a function of annealing temperature. Figure 3 shows the dependence of the reverse breakdown voltage of the diode upon the annealing temperature. A comparison of Figures 2 and 3 shows some definite correlation (except for annealing at 430°C). When the overall deep-energy-level concentration is high, its breakdown voltage is

also correspondingly higher, and vice versa. It seems that thermal treatment at different temperature could alter the overall deep-energy-level concentration. This change is directly reflected by the number of electron traps in the interface between the diode and the gold Schottky contact. More electron traps result in higher resistivity. Consequently, the reverse breakdown voltage is higher as well.

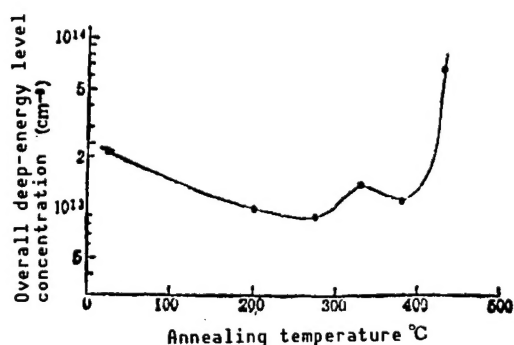


Figure 2. Overall Deep-Energy-Level Concentration vs. Annealing Temperature

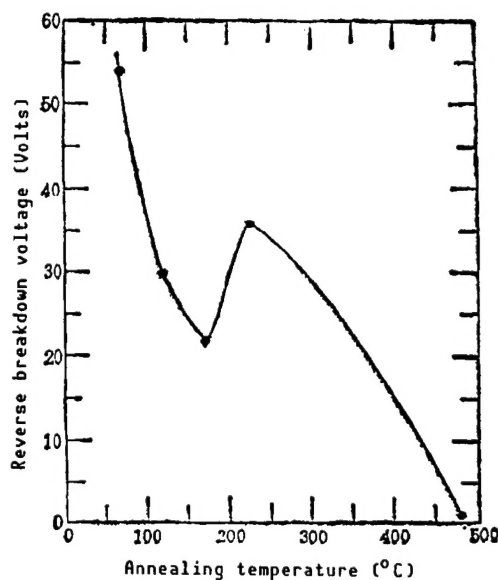


Figure 3. Reverse Breakdown Voltage of the Diode vs. Annealing Temperature

These results indicate that the complex thermal reaction between gold and the high-purity MBE-grown GaAs layer has a significant effect on the measurement of its deep energy level.

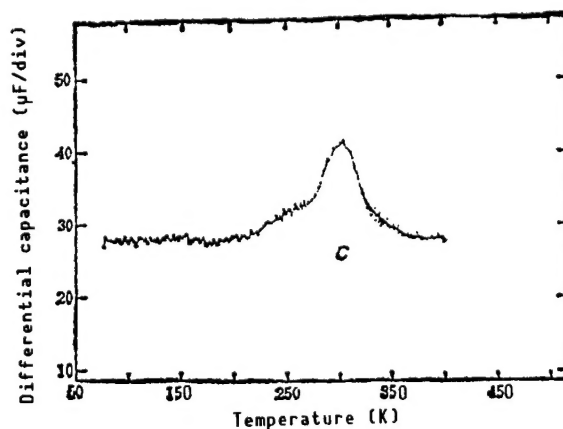


Figure 4. DLTS Spectrum of Diode Annealed at 430°C After Mesa-Etching

Finally, the diode annealed at 430°C was etched in  $\text{H}_2\text{SO}_4:\text{H}_2\text{O}_2:\text{H}_2\text{O} = 1:1:18$  for 7 minutes to form a mesa diode, whose DLTS spectrum was then measured, as shown in Figure 4. Only one of the three original peaks, i.e., peak C, showed up; other peaks disappeared. The results of this lead us to believe that the annealing reaction introduced certain energy-level peaks and the reaction products were primarily located at the outside.<sup>7</sup> Once these reaction products are etched away by the mesa-etching process, the peaks also disappear. The presence of this reaction product has been confirmed through microscopic observation during the annealing process. It seems reasonable to believe that 0.63 eV is an intrinsic deep energy level in the high-purity GaAs film grown under an arsenic-rich condition.

#### IV. Conclusion

1. A series of DLTS spectra has been obtained with diodes made of MBE-grown high-purity GaAs with gold Schottky contacts. It has been found that the thermal reaction between gold and the MBE-grown high-purity GaAs thin film has a significant effect on its deep energy level and can affect the accurate determination of its deep energy level.
2. There is a relation between the overall deep-energy-level concentration at different annealing temperature and the reverse breakdown voltage of the diode.

The authors wish to thank Mr Lannet for his assistance in preparing the high-purity MBE-grown GaAs thin film and Mr Johan for his technical assistance.

#### References

1. F. Chekir, C. Barret, and A. Vapaille, J. APPL. PHYS., Vol 54, 1983, p 6474.
2. W.G. Petro, I.A. Babalola, T. Kendelewicz, I. Lindau, and W.E. Spicer, J. VAC. SCI. TECHNOL., Vol A., 1983, p 1181.
3. J.R. Waldrop, APPL. PHYS. LETT., Vol 41, 1982, p 350.
4. D.V. Lang, A.Y. Cho, A.C. Gossard, M. Ilegems, and W. Wiegmann, J. APPL. PHYS., Vol 47, 1976, p 2558.
5. M. Hansen, "Constitution of Binary Alloys," McGraw-Hill, New York, 1958.
6. J. Gyulai and J.W. Mayer, J. APPL. PHYS., Vol 42, 1971, p 3578.
7. N. Newman, W.G. Petro, T. Kendelewicz, S.H. Pan, S.J. Eglash, and W.E. Spicer, Ibid., Vol 47, 1985, p 1247.

## **GaAlAs/GaAs SQW SCH Laser Diode Fabricated by MOCVD**

90FE0052B Beijing BANDAOTI XUEBAO [CHINESE JOURNAL OF SEMICONDUCTORS] in Chinese Vol 10 No 12, Dec 89 (MS Received 4 May 89) pp 960-964

[Article by Zhuang Wanru [8369 1238 1172], Shi Zhiwen [4258 1807 2429], and Yang Peisheng [2799 1014 3932] of the Institute of Semiconductors, the Chinese Academy of Sciences, Beijing, and M. Umeno, T. Soga, and T. Jimbo of the Department of Electrical and Computer Engineering, Nagoya Institute of Technology, Nagoya, Japan (the MOCVD was performed in Umeno's lab at Nagoya Institute of Technology and the lasers were fabricated and characterized at the Institute of Semiconductors): "GaAlAs/GaAs SQW SCH Laser Diode Fabricated on Si by MOCVD"; project funded by National Natural Science Foundation]

### **[Text] Abstract**

GaAlAs/GaAs SQW (single quantum well) epitaxial layers with SLS (strained-layer superlattices) are grown on Si by MOCVD (metal-organic chemical vapor deposition). A proton-bombardment isolation technique is used to fabricate 10- $\mu$ m stripe-geometry SQW laser diodes. Emission is observed at room temperature after excitation by a pulse current (1  $\mu$ s wide at 20 kHz). The lowest threshold current is 92 mA and the laser wavelength is 849.2 nm. The external differential quantum efficiency is 11 percent.

**Key Words:** semiconductor laser, optoelectronic integrated circuit (OEIC), nonstoichiometric heteroepitaxy, GaAs grown on Si.

### **I. Introduction**

The heteroepitaxial growth of GaAs on Si (GaAs/Si) has attracted a great deal of interest since the 1980's. Although there are still many problems, there have been reports on the successful development of LED's (light emitting diodes), lasers, FET's (field effect transistors), and solar cells.

Silicon is the most mature material for device fabrication. In LSI (large-scale integration) and VLSI (very large-scale integration), silicon is the principal material. Gallium arsenide has advantages such as a direct band-gap structure, high mobility, high drift velocity, and ease of obtaining better heterostructures. It is an important substrate material for optoelectronic

devices, microwave devices, and high-speed devices. If high-quality GaAs can be grown on Si, it may be possible to combine the advantages of silicon and gallium arsenide and avoid their individual shortcomings. optoelectronic, microwave, and high-speed devices are fabricated on GaAs, and VLSI circuits are fabricated on Si; this integrates several devices on one chip. It is even possible to develop new functional components. A GaAs/Si single optoelectronic integrated chip involves the fabrication of optoelectronic devices (such as lasers, LED's or optical detectors) and high-speed electronic devices (such as FET's, HEMT's [high electron mobility transistors], etc.) on GaAs and VLSI circuits on Si.<sup>1</sup> This type of chip can be used in a local network for fiber-optic communications in the near future. The next step is to make the optical link between silicon VLSI chips (to simplify the network structure by using optical switches). Single-crystal silicon substrate is also large in size and low in cost.

T.H. Windhorn and R. Fisher have separately reported the successful fabrication of GaAlAs/GaAs double heterojunction (DH) lasers on Si using the MBE method and a two-step process, respectively.<sup>2,3</sup> R.D. Dupuis was able to grow a transition layer on Si by MOCVD to fabricate a quantum well laser.<sup>4</sup> S. Sakai, et al., also grew an SLS transition layer on Si by MOCVD and fabricated DH and quantum well lasers.<sup>5</sup> These lasers were found to exhibit pulse emission at room temperature. D.G. Deppe and D.C. Hall have used MBE and a two-step MOCVD method to fabricate room-temperature continuous-wave (CW) lasers on Si. The lifetime was 4 hours in 1987<sup>6</sup> and was improved to 10 hours in 1988.<sup>7</sup> In the present work, GaP/GaAs<sub>0.5</sub>P<sub>0.5</sub> and GaAs<sub>0.5</sub>P<sub>0.5</sub>/GaAs SLS transition layers are grown on Si by MOCVD. This is followed by growth of an SQW laser structure and forming high-resistance isolation by proton bombardment to produce 10- $\mu$ m wide stripe-geometry lasers. Laser emission at room temperature is observed.

## II. Growing GaAs on Si With SLS

The major problems encountered in growing GaAs on an Si substrate are 1) there is a  $10^{12}\text{cm}^{-2}$  mismatch dislocation at the GaAs/Si interface because the lattice constant of GaAs is different from that of Si by 4 percent; 2) since the thermal expansion coefficient of GaAs is more than twice that of Si, the GaAs epitaxial layer is under  $10^9$  dyne $\cdot$ cm<sup>-2</sup> of strain, which not only affects the performance of the device but also causes the wafer to warp; and 3) when a polar semiconductor is grown on top of a nonpolar semiconductor, it is easy to have some inverted structure at the interface, such as some Ga-Ga or As-As bond. In order to overcome this inverted structure, the substrate must be off from (100) by 2-5°.

The following methods have been used to grow GaAs on Si epitaxially. 1) Use of Ga as an intermediate transition layer.<sup>8</sup> However, it was discovered recently that Ga would diffuse into the epitaxial layer, which results in spontaneous doping. 2) The most common method is a "two-step growth method"<sup>9</sup>: the first step is to deposit a very thin (approximately 20 nm) amorphous GaAs layer at high temperature by MBE and then anneal it at 450-500°C to convert the GaAs to single crystal. Afterward a GaAs layer can be grown at normal temperature by MBE or MOCVD. 3) Use an SLS layer as a transition layer. An SLS is the alternate growth of two mismatched thin heterolayers. When the layer thickness

is less than its critical thickness, the lattice strain can compensate for the lattice mismatch, thus greatly reducing the mismatch location.

In this work, the SLS was used to reduce the stress caused by the lattice mismatch. Researchers usually use a GaAlAs/GaAs or AlGaAsP/AlP SLS to be transformed into an AlGaAsP/GaAs SLS layer. In order to avoid the chemical instability associated with Al, we first grew a thin GaP layer (GaP has a lattice constant close to that of Si and has a thermal expansion coefficient close to that of GaAs). Then, it gradually transforms from GaP toward GaAs, i.e., from a GaP/GaAs<sub>0.5</sub>P<sub>0.5</sub> SLS to a GaAs<sub>0.5</sub>P<sub>0.5</sub>/GaAs SLS. The GaAs layer can be grown on top of it. From deep level and stress measurements, it was found that such an SLS structure has a significantly improved material integrity.<sup>10,11</sup>

In order to grow GaAs on Si, first we had to remove the oxide layer from the silicon surface. To this end, we baked the silicon wafer in H<sub>2</sub> + PH<sub>3</sub> for 10 minutes at 900–1000°C to allow the residual surface oxide to be reduced to a gaseous phase and be carried away by the gas flow. In addition, a very thin layer of phosphorus was deposited on the Si to facilitate the growth of GaP.

In this work, a multilayer structure, as shown in Figure 1, was grown on a piece of n-type (100) Si substrate at a 2° angle toward (110). The typical growth process is to first bake the silicon wafer in H<sub>2</sub> + PH<sub>3</sub> for 10 minutes at 950°C and then to put on a 50-nm layer of GaP at 900°C. Then, five periods of GaP/GaAs<sub>0.5</sub>P<sub>0.5</sub> (each layer 20 nm thick) and five periods of GaAs<sub>0.5</sub>P<sub>0.5</sub>/GaAs (each layer 20 nm thick) were grown at 680°C. These super-thin layers formed the SLS structure. Then, a 2-μm n<sup>+</sup> GaAs buffer layer was grown on top of it at 650°C. Afterward, it was heated and cooled five times from 650°C to 200°C to form a thermal-stress buffer layer to help absorb some defects.<sup>7</sup>

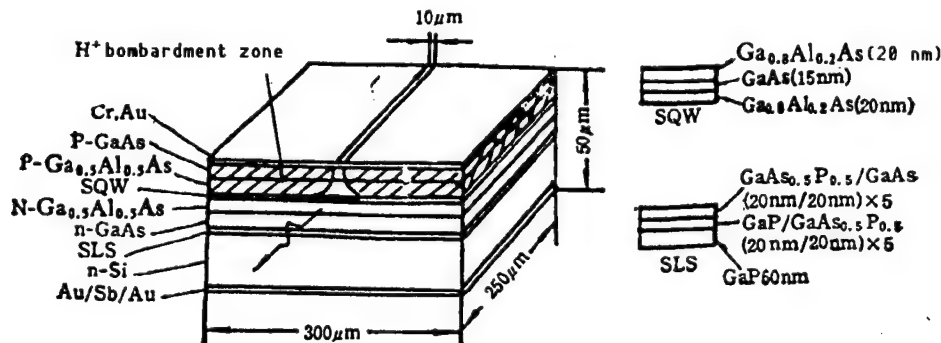


Figure 1. Schematic Diagram of SQW Laser Diode Structure on Si Substrate

### III. Fabrication of SQW Laser

After the thermal cycle treatment, a 1-μm thick Se-doped N-type Ga<sub>0.5</sub>Al<sub>0.5</sub>As confinement layer (concentration  $1 \times 10^{17} \text{ cm}^{-3}$ ) was grown on top of it in the same MOCVD reaction chamber. This was followed by growth of the SQW structure, which was formed by a 15-nm thick intrinsic GaAs potential well and a 20-nm thick Ga<sub>0.5</sub>Al<sub>0.5</sub>As potential barrier on either side. On top of this, a 1-μm



thick Zn-doped P-type  $\text{Ga}_{0.5}\text{Al}_{0.5}\text{As}$  confinement layer (concentration  $1 \times 10^{18}\text{cm}^{-3}$ ) and a  $2\text{-}\mu\text{m}$  thick P-type GaAs top layer (concentration  $5 \times 10^{18}\text{cm}^{-3}$ ) were deposited.

In order to obtain good ohmic contacts on the p surface, Zn was diffused at  $650^\circ\text{C}$  to raise its surface concentration to  $1 \times 10^{20}\text{cm}^{-3}$ . The silicon substrate was ground down to a total overall thickness of approximately  $60\text{ }\mu\text{m}$ . Au/Sb/Au was evaporated onto the n side and Cr and Au were evaporated on the p side as electrical contacts. High-resistance isolation was achieved by proton bombardment to yield  $10\text{-}\mu\text{m}$  wide stripe-geometry laser diodes.<sup>12</sup> A  $250\text{-}\mu\text{m}$  long resonance cavity was fabricated by the cleavage technique and the P-side of the diode was placed face down on a copper heat sink.

#### IV. SQW Laser Characteristics

At room temperature (295 K), a pulse current (20 kHz frequency,  $1\text{-}\mu\text{s}$  pulse width) was applied to the laser and laser emission was observed upon excitation. Figure 2 shows the F64 laser diode power output as a function of impressed current (L-I [inductance current] characteristics). Its threshold current  $I_{th}$  was 92 mA and the corresponding threshold current density was  $3.7 \times 10^3\text{A}\cdot\text{cm}^{-2}$ . The external differential quantum efficiency  $\eta_d$  is 11 percent. Nevertheless, the L-I curve decays rapidly with time. The threshold current increased rapidly with time and the light output decreased significantly. The external differential quantum efficiency also dropped off with time. The reverse I-V (current-voltage) characteristics also changed significantly. After 15 minutes, the laser characteristics were no longer obvious.

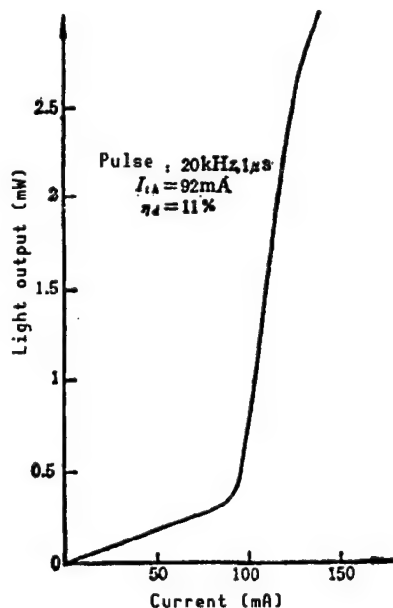


Figure 2. Light Power Output vs. Current for SQW Laser F64

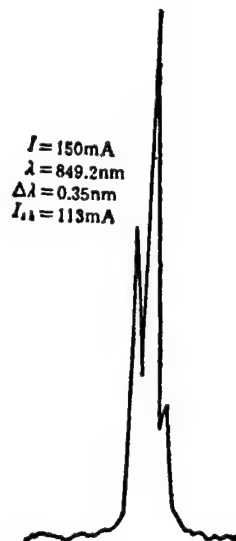


Figure 3. Pulse Emission Spectrum of SQW Laser F35



The emission spectrum of Laser F35 excited under the above pulse condition is shown in Figure 3. The peak wavelength is 849.2 nm and the spectral half width is 0.35 nm.

## V. Discussion

Based on this experiment, we have reached the following conclusions:

1. The use of an SLS is effective in improving the quality of GaAs grown on Si. The GaAs/[GaAs<sub>0.5</sub>P<sub>0.5</sub> (SLS)]/[GaAs<sub>0.5</sub>P<sub>0.5</sub>/GaP (SLS)]/GaP/Si structure can yield better quality GaAs. The SQW lasers fabricated on it were able to emit laser pulses at room temperature.
2. The SQW laser developed was only found to emit laser pulses at room temperature. Continuous-wave laser emission at room temperature was not achieved. The threshold current was high and the power output and quantum efficiency were low. Especially, the laser performance deteriorated rapidly. These facts indicate that there are many defects and considerable stress in the source region of the laser. The quality of GaAs needs further improvement.
3. Based on a computation of the GaAs/Ga<sub>0.8</sub>Al<sub>0.2</sub>As square well,<sup>13</sup> the wavelength of the SQW laser should be 860 nm (the laser wavelength of the SQW laser grown on GaAs under identical MOCVD conditions is close to the calculated wavelength). However, the measured wavelength is 849.2 nm which is 10 nm less than the calculated value. This issue needs to be further investigated.
4. The primary issue associated with fabricating a GaAs/GaAlAs laser on Si is that the quality of the mismatched heteroepitaxial GaAs layer must be further improved. With further investigation and improvement of the technique, the integrity of the Si/GaAs interface will be better. Stress may be further relieved by additional heat treatment cycles.<sup>7</sup> In the near future, the performance of the GaAs/GaAlAs laser fabricated on an Si substrate will gradually improve to meet the requirements for practical applications.

## References

1. S. Sakai and M. Umeno, JPN. J. APPL. PHYS., Vol 24, 1985, p L666.
2. T.H. Windhorn and G.M. Metze, APPL. PHYS. LETT., Vol 47, 1985, p 1031.
3. R. Fisher, et al., Ibid., Vol 48, 1986, p 1360.
4. R.D. Dupuis, et al., Ibid., Vol 50, 1987, p 407.
5. S. Sakai, H. Siraishi, M. Umeno, IEEE J. QUANTUM ELECTRONICS, Vol QE-23, 1987, p 211.
6. D.G. Deppe, et al., APPL. PHYS. LETT., Vol 51, 1987, p 1271.

7. D.C. Hall, D.G. Deppe, et al., J. APPL. PHYS., Vol 64 No 6, 1988, p 2854.
8. R.P. Gale, et al., IEEE ELECTRON DEVICE LETT., Vol EDL-2, 1981, p 169.
9. M. Akiyama, et al., J. CRYST. GROWTH, Vol 68, 1984, p 21.
10. T. Soga, et al., JPN. J. APPL. PHYS., Vol 25 No 10, 1986, p 1510.
11. Ibid., Vol 25 No 11, 1986, p 1680.
12. Wang Qiming [3769 0796 2494] and Zhuang Wanru, BANDAOTI XUEBAO [CHINESE JOURNAL OF SEMICONDUCTORS], Vol 1 No 1, 1980, p 46.
13. R. Dingle, et al., PHYS. REV. LETT., Vol 33, 1974, p 827.

## RTA of Si and As Dual Implantation Into GaAs

90FE0052C Beijing BANDAOTI XUEBAO [CHINESE JOURNAL OF SEMICONDUCTORS] in Chinese Vol 11 No 2, Feb 90 (MS Received 20 Jan 89) pp 140-143

[Article by Zhu Dehua [2612 1795 5478], Li Guohui [2621 0948 6540], Zhang Tonghe [1728 6639 0735], and Wang Yuqi [3769 3768 3823] of the Institute of Low-Energy Nuclear Physics, Beijing Teachers' University, and Sun Guiru [1327 6311 1172] of the Ministry of Metallurgical Industry's General Institute of Nonferrous Metals, Beijing: "Study of RTA Involving Dual Implantation of Si and As Into GaAs"]

### [Text] Abstract

Rapid thermal annealing (RTA) of Si-implantation into GaAs is studied. The optimum annealing condition is 930-950°C for 5 seconds. Electron concentration is found to be saturated when the implantation dose exceeds  $10^{13}\text{cm}^{-2}$ . In order to raise the electron concentration, dual implantation of Si and As into GaAs is proposed in this work. Electrical characteristics are measured under implantation conditions over the range of (60-80) keV,  $(5-10) \times 10^{14}\text{Si/cm}^2$  + (150-180) keV,  $(5-30) \times 10^{14}\text{As/cm}^2$  with RTA. Results clearly show that dual implantation significantly raises the electron concentration. For a sample prepared at 80 keV,  $10^{15}\text{Si/cm}^2$  + 150 keV,  $3 \times 10^{15}\text{As/cm}^2$ , the electron concentration is greater than  $10^{19}\text{cm}^{-3}$ . TEM (transmission electron microscopy) observation shows that the residual defect density is significantly lower than that of single implantation. The compensation mechanism in dual implantation is also discussed.

Key Words: Si, As dual implantation into GaAs; rapid thermal annealing.

### I. Introduction

Si-ion implantation is usually used to prepare an n-type layer in a GaAs device. RTA is highly efficient, has little impurity diffusion, and does not require sealing or As overpressure protection during annealing. Hence, RTA has gradually become an important technique for GaAs IC fabrication.<sup>1</sup> The RTA characteristics associated with Si implantation into GaAs have been reported.<sup>2-5</sup> At a low Si implantation dose of  $(4-10) \times 10^{12}\text{cm}^{-2}$ , the electrical activity is greater than 50 percent. As the dose increases, the carrier

concentration appears to be saturated at approximately  $(2-3) \times 10^{18} \text{cm}^{-3}$ . The cause is due to the mutual interaction between  $[\text{Si}_{\text{Ga}}^*]$ , i.e., Si taking the place of Ga, and  $[\text{Si}_{\text{As}}]$ , i.e., Si taking the place of As, and the mutual interaction between Si and various vacancies. These interactions not only depend on the  $[\text{V}_{\text{Ga}}/\text{V}_{\text{As}}]$  ratio but also on the implantation and annealing conditions.

The implantation of P or As + Si into GaAs at low doses has been reported.<sup>5,7,8</sup> The electrical characteristics of the implanted layer have been improved significantly. RTA of dually implanted ions into GaAs has heretofore not been reported. The objective of this work is to use dual implantation of Si + As, as well as RTA, to raise the carrier concentration in the GaAs.

## II. Experimental Apparatus and Method

A single-crystal wafer of In LEC-Si [indium liquid-encapsulated-Czochralski-grown silicon]-GaAs was chosen. After mechanical polishing and chemical etching, it was implanted using the 400-keV ion-implantation equipment at Beijing Teachers' University. RTA was carried out in a Chinese-made KST-1 white-light rapid annealing furnace.<sup>10</sup> Samples were annealed face-to-face in a protective  $\text{N}_2$  atmosphere. The electrical properties of the implantation layer were measured by van der Pauw's method and the differential Hall technique. The residual defect in the implantation layer was observed by TEM.

## III. Experimental Results and Discussion

### 1. RTA of Si Implantation Into GaAs

Figures 1(a) and 1(b) show the surface carrier concentration  $n_s$  and mobility  $\mu_H$  of silicon-implanted GaAs as a function of annealing temperature and annealing time, respectively. It was found that  $n_s$  and  $\mu_H$  essentially follow the same pattern over a variety of implantation conditions. They both reached a maximum when annealing was done at 930–960°C for 5 seconds. This indicates that the activation impurity and recovery of lattice damage take place simultaneously during RTA. Raising the annealing temperature and time appropriately favors the recovery of lattice damage and impurity activation. Therefore, both  $n_s$  and  $\mu_H$  begin to increase with higher annealing temperature and longer annealing time. However, because Si is an amphoteric element, Tiku<sup>9</sup> believes that there is a higher probability for Si to take the place of As. Thus, the donor is compensated and  $n_s$  decreases. On the other hand, because of the surface decomposition of GaAs,  $\mu_H$  decreases. Hence, raising the annealing temperature and lengthening the annealing time further would cause  $n_s$  and  $\mu_H$  to decline.

### 2. Dependence of Electron Concentration Upon Implantation Dose

Under the optimum annealing condition (960°C, 5 s), the relation between the Si implantation dose into GaAs at 180 keV and  $n_s$  was investigated. Our results show that below  $10^{12} \text{cm}^{-2}$ ,  $n_s$  is linear with implantation dose. However, when the implantation dose exceeds  $10^{12} \text{cm}^{-2}$ ,  $n_s$  and the implantation dose deviate from

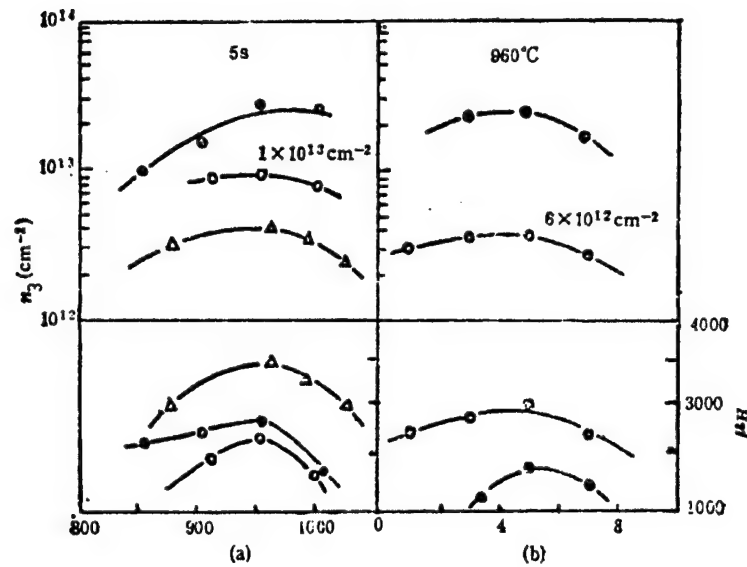


Figure 1.  $n_s$  and Mobility  $\mu_H$  vs. (a) Annealing Temperature and (b) Annealing Time  
 •: 80 keV  $1 \times 10^{14} \text{cm}^{-2}$ ;  $\Delta$ : 120 keV  $6 \times 10^{12} \text{cm}^{-2}$ ; o: 180 keV

a straight line. When the implantation dose reaches  $2.5 \times 10^{13} \text{cm}^{-2}$ ,  $n_s$  is saturated.

### 3. Dual Implantation Electrical Characteristics

The optimum annealing conditions for dual implantation are still  $960^\circ\text{C}$  and 5 s. The results are shown in Table 1. The electrical characteristics of dually implanted GaAs were measured over a range of (60–80) keV,  $(5\text{--}10) \times 10^{14} \text{Si/cm}^2 + (150\text{--}180) \text{ keV}, (5\text{--}30) \times 10^{14} \text{As/cm}^2$  after annealing for 5 s at  $960^\circ\text{C}$ . The results are shown in Table 2. It is found that the electron concentration increases and resistivity decreases significantly as a result of dual implantation within the above dose range. However, results from ion implantation into GaAs vary from place to place.

Table 1. Electrical Characteristics of 80 keV,  $5 \times 10^{14} \text{Si/cm}^2 + 180 \text{ keV}, 2 \times 10^{15} \text{As/cm}^2$  Implantation Into GaAs, Annealed for 5 s

Electrical parameter	Temperature $^\circ\text{C}$		
	900	960	1000
$n_s \text{ (cm}^{-2}\text{)}$	$1.3 \times 10^{13}$	$5 \times 10^{13}$	$2.0 \times 10^{13}$
$\mu_H \text{ (cm}^2/\text{V}\cdot\text{S)}$	1873	810	1610
$\rho_s \text{ (}\Omega/\square\text{)}$	257	154	194

Table 2. 80 keV,  $1 \times 10^{15}\text{Si}/\text{cm}^2$  + 150 keV As Implantation Into GaAs, Annealed for 5 s at  $960^\circ\text{C}$

Mate- rial	1				2			
As dose ( $\text{cm}^{-2}$ )	Sam- ple #	$n_s(\text{cm}^{-2})$	$\mu_H(\text{cm}^2/\text{V}\cdot\text{S})$	$\rho$ , ( $\Omega/\square$ )	Sam- ple #	$n_s(\text{cm}^{-2})$	$\mu_H(\text{cm}^2/\text{V}\cdot\text{S})$	$\rho$ , ( $\Omega/\square$ )
0	87-1	$2.4 \times 10^{13}$	989	268	87-4	$2.9 \times 10^{13}$	1651	155
$1 \times 10^{15}$	87-2	$4.7 \times 10^{13}$	1219	111	87-5	$5.3 \times 10^{13}$	1034	115
$3 \times 10^{15}$	87-3	$9.4 \times 10^{13}$	831	81	87-6	$2.6 \times 10^{14}$	616	39

#### 4. Cross Section of Electron Concentration

Specimen 87-6 has the highest  $n_s$  and lowest  $\rho_s$ . Its electron concentration distribution is shown in Figure 2. Its peak concentration is as high as  $3 \times 10^{19}\text{cm}^{-3}$ .

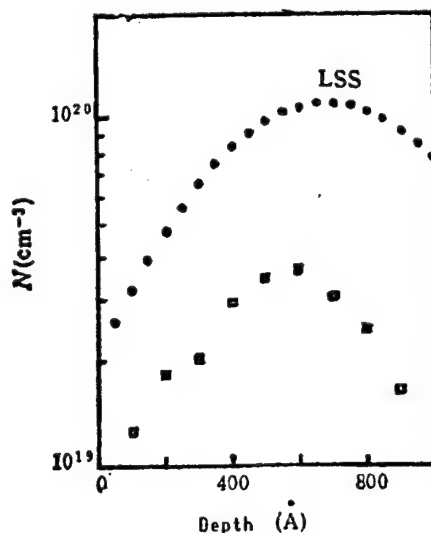


Figure 2. Electron Concentration Distribution

•: LSS theoretical value  
□: Experimental data

#### 5. Residual Defect Analysis

Figures 3(a) and 3(b) [photographs not reproduced] are the TEM pictures for specimens 88-1 (60 keV,  $1 \times 10^{15}\text{Si}/\text{cm}^2$ ) and 88-22 (60 keV,  $1 \times 10^{15}\text{Si}/\text{cm}^2$  + 150 keV,  $3 \times 10^{15}\text{As}/\text{cm}^2$ ). It is found that the residual defect density of the dual implantation specimen is far lower than that of the single implantation specimen. The implanted As could more effectively replace Ga to form SiGa. On

the other hand, it also reduces the formation of complexes associated with  $V_{As}$  (such as  $Si_{Ga}V_{As}$ ,  $Si_{Ga}Si_{As}$ , etc.). Thus, the residual defect density is greatly lowered.

## VI. Conclusion

1. The optimum RTA conditions for Si implantation into GaAs are 930~960°C and 5 s.
2. As the implantation dose increases, the electron concentration of Si in GaAs approaches saturation.
3. Dual implantation can significantly raise the electron concentration, approaching  $3 \times 10^{19} \text{cm}^{-3}$ , and can drastically reduce the residual defects.

## References

1. S.J. Pearson, et al., J. ELECTROCHEM. SOC., Vol 132, 1985, p 2743.
2. H. Kanber, et al., J. APPL. PHYS., Vol 57, 1985, p 4732.
3. S.J. Pearson, et al., Ibid., Vol 48, 1986, p 38.
4. H. Kanber, et al., Ibid., Vol 47, 1985, p 120.
5. M.E. Greiner, et al., Ibid., Vol 57, 1985, p 5186.
6. T.C. Banwell, et al., J. PHYS. CHEM. SOLID., Vol 44, 1983, p 527.
7. H. Kroetle, NUCL. INSTR. METHODS, Vols 182/183, 1981, p 625.
8. A.R. Von. Neida, et al., APPL. PHYS. LETT., Vol 49, 1986, p 1708.
9. S.K. Tiku, J. ELECTROCHEM. SOC., Vol 132, 1985, p 2237.
10. Zhang Tonghe, et al., BEIJING SHIFAN DAXUE XUEBAO [JOURNAL OF BEIJING TEACHERS' UNIVERSITY] (Natural Science Edition), Vol 3, 1987, p 41.

## **In-Situ Monitoring of High-Quality Diffraction Gratings**

90FE0052D Beijing BANDAOTI XUEBAO [CHINESE JOURNAL OF SEMICONDUCTORS] in Chinese Vol 11 No 2, Feb 90 (MS Received 23 Nov 88) pp 153-157

[Article by Xie Jianping [6200 1696 1627] and Ming Hai [2494 3189] of the Department of Physics, University of Science and Technology of China, Hefei, and Kunio Tada of the Department of Electronic Engineering, University of Tokyo: "Analysis of Real-Time Monitoring in the Fabrication of High-Quality Diffraction Gratings on a GaAs Substrate"]

### **[Text] Abstract**

High-quality optical gratings can be fabricated on GaAs by in-situ monitoring on the diffraction light intensity in photolithography. This paper focuses on the analysis of the variation of diffraction light intensity as a function of image development and shows the optimal endpoint. The analysis is in good agreement with experimental results.

**Key Words:** monitoring, optical grating, GaAs.

### **I. Introduction**

GaAs is an important material used in integrated optical circuits. It can be used to generate, modulate, and detect light.<sup>1</sup> Fabricating a diffraction grating on GaAs has a significant effect on the making of optical devices such as the distributed feedback (DFB) laser diode, the distributed Bragg reflector (DBR) laser diode, and the optical coupler. The period of this type of grating is of submicron level and cannot be obtained by mechanical engraving or planar semiconductor lithography<sup>2</sup>; most of these gratings are made by holographic lithography.

The laser beam from a short-wavelength laser, such as a He-Cd laser, is split into two. The two light beams enter the surface of GaAs coated evenly with a photoresist layer at a large phase angle. After exposure, development and etching, a submicron-period grating can be fabricated on the GaAs surface. It is most difficult to ensure the reproducibility and high quality of the grating on GaAs by holographic photolithography. One of the authors<sup>3</sup> has used in-situ monitoring of diffraction light intensity to control the degree of



development to fabricate a 255-nm high-quality diffraction grating on GaAs by photolithography. The objective of this work is to analyze how diffraction light intensity varies with the degree of development of the photoresist and use it to determine the optimal endpoint in order to improve the reproducibility in the fabrication of gratings and to raise the yield of integrated optical devices. In addition, the variation of diffraction light intensity as a function of degree of etching is also studied on a preliminary basis.

## II. Experiment and Analysis

Straight interference fringes with a sinusoidal intensity distribution were obtained with a He-Cd laser at  $\lambda = 3250 \text{ \AA}$  in order to expose the photoresist (MPS1400-17) on a GaAs substrate. Real-time monitoring was done in the developing tank. The developing solution was Microposit developer:  $\text{H}_2\text{O} = 1:1$ , with an index of refraction  $n = 1.338$ . A He-Ne laser beam ( $\lambda = 6328 \text{ \AA}$ ) was used for monitoring: it entered the solution at an incidence angle of  $72^\circ$  and the first-order diffraction was monitored with a photocell at  $65^\circ$  on the same side of the normal line and recorded on an xy recorder. Figure 1 shows a typical curve of first-order light intensity with developing time; it includes the diffraction peaks. At the second peak, the diffraction efficiency is approximately 4 percent and at the first peak the efficiency is slightly under 0.6 percent. Experiments have shown<sup>3</sup> that excellent grating masks can be obtained if development is terminated at the second when the diffraction light intensity reaches the second peak. The width of the exposed stripes on the GaAs substrate is approximately one-half of the period of the grating. Optimal results can be obtained by transferring the grating pattern on the photoresist onto the GaAs substrate by ion etching. The advantages of this technique include factors such as lack of criticality in the photoresist thickness, in the amount of holographic exposure, and in the developing conditions for ensuring the quality of the grating mask. In addition, the quality of the grating will not be affected by overetching by monitoring the etching process. The variation of diffraction light intensity with developing time as a result of in-situ monitoring is analyzed as follows in order to identify the optimal endpoint.

The grating pattern gradually takes shape in the development process according to the sinusoidal exposure distribution on the photoresist. The height fluctuation of the photoresist  $h(t)$  increases with developing time and finally approaches saturation. Correspondingly, the intensity of the first-order diffraction also reaches a maximum with  $h(t)$  to form the first diffraction peak. Due to the absorption of light by the photoresist, the amount of exposure decreases exponentially with the depth of the photoresist layer; therefore, we can assume that  $h(t)$  increases according to a negative exponential pattern. The maximum value of  $h(t)$ , i.e.,  $h_m$ , and the required developing time  $t_1$ , are determined by the beam ratio of the two interference beam and the developing conditions. In Figure 1,  $t_1$  is approximately 5 s. The He-Ne laser beam with an amplitude  $A_0$  reaches the photoresist at an incident angle of  $\alpha_1$  and refracts upward along the direction of  $\alpha_2$  (as shown in Figure 2(a)). Let us use point A ( $x = 0$ ) as a reference for the diffraction light phase angle.

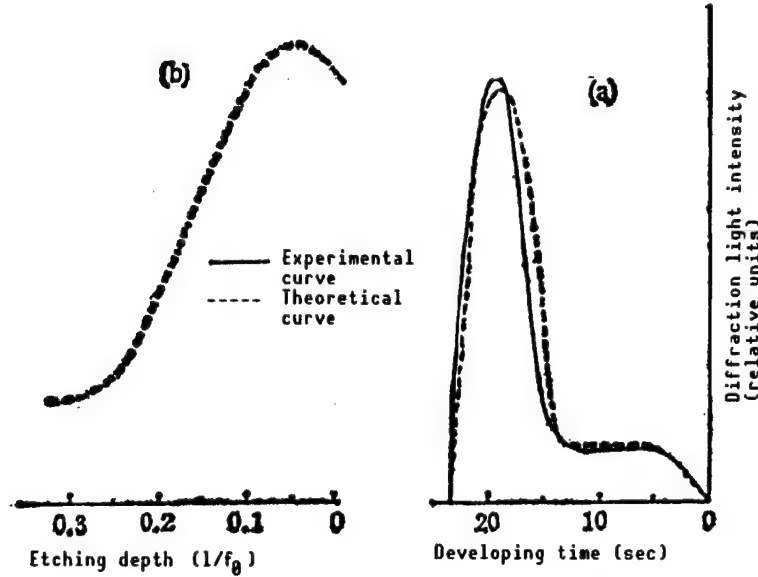


Figure 1. Diffraction Light Intensity Vs. Degree of (a) Developing Time  
(b) Etching Depth

At  $x$ , i.e., point B, the phase angle is  $\frac{2\pi}{\lambda}(BC-AC')$ . Draw lines  $BB'$  perpendicular to the  $x$ -axis from  $x$  and draw  $B'D'$  and  $B'D$  perpendicular to the incident and diffraction light, respectively.  $BB'$  is the depth of the photoresist at  $x$ , which is  $\frac{1}{2}h(t)\sin 2\pi f_0 x$ , where  $\frac{1}{f_0}$  is the period of the grating. From Figure 2 we know that  $BC = D'C + BD' = x \sin \alpha_1 + \frac{1}{2}h(t)\sin 2\pi f_0 x \cos \alpha_1$ . Similarly,  $AC' = x \sin \alpha_2 - \frac{1}{2}h(t)\sin 2\pi f_0 x \cos \alpha_2$ . Thus, the diffraction light amplitude across a width of  $dx$  at B is

$$u(x) dx = A_0 \rho_1 e^{j \frac{m}{2} \sin 2\pi f_0 x} e^{j 2x \left( \frac{\sin \alpha_1}{\lambda} - \frac{\sin \alpha_2}{\lambda} \right)} dx \quad (1)$$

where  $\rho_1$  is the reflection coefficient of the photoresist,  $\lambda$  is the wavelength of the He-Ne laser in the developer, and  $\frac{m}{2} = \frac{2\pi}{\lambda} h(t) (\cos \alpha_1 + \cos \alpha_2)$ .

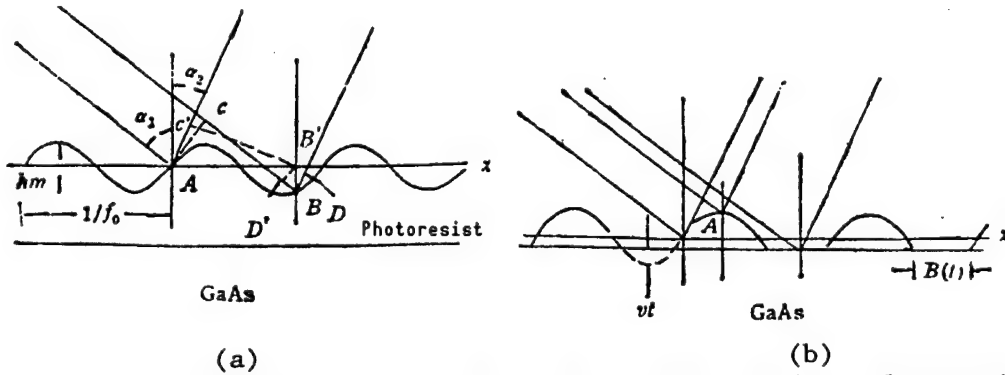


Figure 2. Phase distribution Caused by Photoresist Surface Fluctuation  
(a) GaAs surface unexposed; (b) GaAs surface partially exposed

If the effect of beam diameter is neglected, then the diffraction light amplitude along  $\alpha_2$  can be obtained by integrating equation (1),

$$\begin{aligned} u(\alpha_2) &= \int_{-\infty}^{\infty} u(x) dx \\ &= \int_{-\infty}^{\infty} A_0 \rho_1 e^{j \frac{m}{2} \sin 2\pi f_0 x} e^{-j 2\pi \left( \frac{\sin \alpha_2}{\lambda} - \frac{\sin \alpha_1}{\lambda} \right) x} dx \end{aligned} \quad (1')$$

The direction and intensity of the first-order component of Fraunhofer diffraction are<sup>4</sup>:

$$\sin \alpha_2 = \lambda \left( f_0 - \frac{\sin \alpha_1}{\lambda} \right), I_1 = A_0^2 \rho_1^2 J_1^2 \left( \frac{m}{2} \right). \quad (2)$$

where  $J_1$  is a first-order Bessel function. In our experiment,  $\alpha_1 = 72^\circ$ ,  $\frac{1}{f_0} = 2550 \text{ \AA}$  and the refractive index of the developer is 1.338. Therefore,  $\alpha_2 \approx 65^\circ$  which is on the same side as the incident light. Furthermore the refractive index of the photoresist is 1.50,  $\rho_1^2 = 0.099$ . The transmittance of the He-Ne light twice across the wall of the developer tank is 0.88. From Figure 1 we know that the efficiency of the first diffraction peak is 0.56 percent, therefore,  $J_1^2 \left( \frac{m}{2} \right) = 0.25$ . The phase modulation of the grating  $\frac{m}{2} = 0.524$  and the maximum fluctuation of the photoresist  $h_m = 0.114 \lambda$ . Previously, we have already assumed that  $h(t)$  increases according to

$$h(t) = h'(1 - e^{-0.5t}) \quad (3)$$

When  $t = 5$  seconds,  $h(t) = h_m$ . Then,  $h' = 0.124 \lambda$ . The calculated values of the first-order diffraction light intensity as a function of time are shown as the dotted line in Figure 1. This dotted line is in good agreement with the experimental curve.

After reaching maximum modulation, the degree of modulation and diffraction light intensity are considered to remain approximately constant with increasing developing time until the photoresist valley reaches the GaAs surface. If the development process is continued, the high reflectivity of the GaAs surface would rapidly raise the diffraction light intensity. The photoresist layer keeps on getting thinner until the grating disappears. The diffraction light intensity rapidly decreases until the second diffraction peak emerges. During this process, the diffraction light intensity is the sum of diffraction from the sinusoidal grating and the GaAs surface stripe grating exposed to the developer (as shown in Figure 2(b)). Assume the GaAs stripe width exposed to the developer is  $B(t)$ , which is a function of developing time. The centers of these stripes are located at the following positions where  $x$  satisfies

$$x - \left( \frac{n}{f_0} + \frac{3}{4f_0} \right) = 0, \text{ where } n = 0, \pm 1, \pm 2 \dots$$

If the highest point of the photoresist A is used as a reference for the phase of the diffraction light, similar to the analysis shown in Figure 2(a), the phase of the diffraction light at x from the exposed GaAs stripe is

$$\frac{2\pi}{\lambda} (hm-vt) (\cos\alpha_1 + \cos\alpha_2) + \frac{2\pi}{\lambda} (\sin\alpha_1 - \sin\alpha_2)x.$$

Here, v is the rate at which the overall photoresist is getting thinner. After taking the width B(t) and position of the exposed GaAs stripe into account, the amplitude of diffracted light across a width dx at x can be written as

$$\sum_{n=-\infty}^{\infty} A_0 \rho_2 \text{rect} \left[ \frac{x - \left( \frac{n}{f_0} + \frac{3}{4f_0} \right)}{B(t)} \right] e^{j \frac{2\pi}{\lambda} (hm-vt) (\cos\alpha_1 + \cos\alpha_2)} e^{j \frac{2\pi}{\lambda} (\sin\alpha_1 - \sin\alpha_2)x} dx.$$

where  $\rho_2$  is the reflective coefficient of the exposed GaAs surface. Based on the fact that the index of refraction of GaAs is 3.6,  $\rho_2^2 = 0.61$ . The residual sinusoidal grating on the photoresist is also limited to individual stripes. Their width is  $\frac{1}{f_0} - B(t)$  and they are centered at

$$x = \frac{n}{f_0} + \frac{1}{4f_0}, \quad n = 0, \pm 1, \pm 2, \dots$$

The phase distribution is identical to equation (1) with the exception of an extra constant phase term  $\frac{2\pi}{\lambda} \frac{hm}{2} \cdot (\cos\alpha_1 + \cos\alpha_2)$ .

From the above we have

$$u(x) dx = A_0 \left\{ \sum_{n=-\infty}^{\infty} \rho_1 \text{rect} \left[ \frac{x - \left( \frac{n}{f_0} + \frac{1}{4f_0} \right)}{\frac{1}{f_0} - B(t)} \right] e^{j \frac{2\pi}{\lambda} \frac{hm}{2} (\cos\alpha_1 + \cos\alpha_2)} e^{j \frac{m}{2} \sin 2\pi f_0 x} \right. \\ \left. + \sum_{n=-\infty}^{\infty} \rho_2 \text{rect} \left[ \frac{x - \left( \frac{1}{f_0} + \frac{3}{4f_0} \right)}{B(t)} \right] e^{j \frac{2\pi}{\lambda} (hm-vt) (\cos\alpha_1 + \cos\alpha_2)} \right\} e^{j 2\pi \left( \frac{\sin\alpha_1}{\lambda} - \frac{\sin\alpha_2}{\lambda} \right) x} dx \quad (4)$$

From equation (1'), the first-order amplitudes of the first and second part in the above equation are

$$A_1 = A_0 \rho_1 \left( \frac{1}{f_0} - B(t) \right) J_1 \left( \frac{m}{2} \right) e^{j \frac{\pi}{2}} e^{j \frac{2\pi}{\lambda} \frac{hm}{2} (\cos\alpha_1 + \cos\alpha_2)} \quad (5)$$

$$A_2 = A_0 \rho_2 B(t) \text{sinc}[B(t) f_0] e^{j \frac{3\pi}{2}} e^{j \frac{2\pi}{\lambda} (hm-vt) (\cos\alpha_1 + \cos\alpha_2)} \quad (6)$$

When the photoresist layer is thinned out evenly as a function of time, B(t) becomes

$$B(t) = \frac{2}{\pi f_0} \sin^{-1} \left( \frac{\nu t}{hm} \right), \quad 0 \leq \nu t \leq hm \quad (7)$$

Then, the first-order light intensity is

$$I_1 = |A_1 + A_1'|^2 \quad (8)$$

Since  $\rho_1^2$  is less than  $\rho_2^2$ ,  $|A_1'|^2$  represents most of the first-order diffraction light intensity. From the data in Figure 1(a),  $\nu = h_m/9 = 0.0127 \lambda/s$ . The calculated values based on equation (8) are shown as the dotted line in Figure 1(a). They are also in good agreement with the experimental curve.

From the analysis, the highest diffraction light intensity is reached when the exposed GaAs stripe width is one-half of the period of the grating. Hence, experimentally it is possible to obtain a high-quality grating mask with a duty ratio of approximately 1 by terminating the development process when the diffraction light intensity reaches its maximum. High-quality grating patterns can then be engraved on a GaAs substrate using ion beam etching with improved reproducibility.

This in-situ monitoring technique can also be used to control the degree of etching. In this case, it is necessary to use a short-wavelength laser (such as an He-Cd laser) for monitoring. The incident angle should be smaller, such as  $30^\circ$ – $50^\circ$ . When the downward etching depth of the exposed GaAs stripe is  $h(t)$ , the AB part at the bottom is single reflection and the BC part is double reflection (as shown in Figure 3). Their first-order diffraction components are

$$\begin{aligned} u_1 &= A_0 \rho_2 \left[ \frac{1}{2f_0} - 2h(t) \tau g \alpha_1 \right] \text{sinc} \left[ \left( \frac{1}{2f_0} - 2h(t) \tau g \alpha_1 \right) f_0 \right] e^{j \frac{2\pi}{\lambda} h(t) (\cos \alpha_1 + \cos \alpha_2)}, \\ u_2 &= A_0 \rho_2^2 h(t) \tau g \alpha_1 \text{sinc} \left[ h(t) \tau g \alpha_2 \frac{\sin(\alpha_1 - \alpha_2)}{\lambda} \right] e^{j \frac{2\pi}{\lambda} 2h(t) / \cos \left( \frac{\alpha_1 + \alpha_2}{2} \right)} \end{aligned} \quad (9)$$

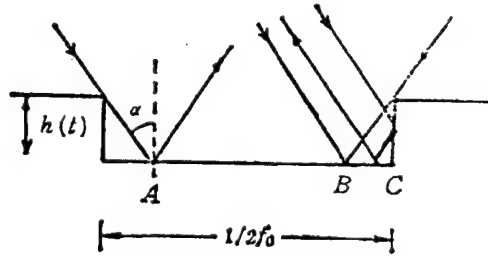


Figure 3. Reflection From the Bottom of the GaAs Trough

Based on earlier analysis, the intensity of first-order diffraction from the grating on the photoresist is less than that from the GaAs grating. Therefore, it can be neglected. Thus, the intensity of diffracted light as a function of etching depth or time is

$$I_1 = |u_1 + u_2|^2 \quad (9')$$

In general,  $h(t) \epsilon g \alpha_1$  is small. In  $u_2$ ,  $\sin c \cdot \left[ h(t) \epsilon g \alpha_1 \frac{\sin(\alpha_1 - \alpha_2)}{\lambda} \right] = 1$ . In equation (9),  $\alpha_1$  and  $\alpha_2$  are the angle of incidence and diffraction, respectively. They are located on either side of the normal line. As an example,  $\lambda = 3250 \text{ \AA}$ ,  $\frac{1}{f_0} = 2550 \text{ \AA}$ ,  $\alpha_1 = \alpha_2 = \alpha = \sin^{-1} \frac{\lambda f_0}{2} = 39.587^\circ$ ,  $\rho_2 = -0.625$ . The data analysis is shown in Figure 1(b). As we can see, when the etching depth  $h(t)$  increases, the diffraction light intensity rises slightly and then declines monotonically. As  $h(t)$  increases further to the point where the incident beam is totally doubly reflected off the GaAs wall, the diffraction light intensity remains unchanged. When  $h(t)$  becomes very deep, the incident light will undergo multiple reflection on the wall and the diffraction light intensity will decrease further to the level equal to the diffraction intensity off the grating on the photoresist.

From Figure 1, it is obvious that using in-situ monitoring of diffraction intensity to control etching is not as effective as using it to control the development process. The quality and reproducibility of an optical grating fabricated on GaAs is primarily determined by the mask. This monitoring technique can be used to effectively produce high-quality masks.

#### References

1. T. Talmill (?) editor, translated by Liang Minji [5328 3046 1015] and Zhang Fuchu [1728 4395 0443], reviewed by Yang Ziahou [2799 0375 0683], "Integrated Optics," Science Publishing House, Beijing, 1982, p 251.
2. R.G. Hansberger (?), translated by Liu Shuqi [0491 2885 2630], et al., "Theory of Integrated Optics," National Defense Industries Publishing House, 1983, p 150.
3. Y. Nakano and K. Tada, OPTICS LETTERS, Vol 13, 1988, p 7.
4. J.W. Goodman (?), translated by Gu Dasan [7357 6671 0005], et al., "Theory of Fourier Optics," Science Publishing House, Beijing, Chapter 4, 1983.

## Hybrid Parabolic-Reflector 2D Surface-Emitting Visible Laser Diode

90FE0052E Beijing BANDAOTI XUEBAO [CHINESE JOURNAL OF SEMICONDUCTORS] in Chinese Vol 11 No 2, Feb 90 (MS Received 21 Jul 89) pp 158-161

[Article by Zhang Xiaobo [1728 0879 3134], Du Guotong [2629 0948 0681], and Gao Dingsan [7559 7307 0005] of the Department of Electronics, Jilin University at Changchun: "Hybrid Parabolic-Reflector Two-Dimensional Surface Emitting Visible Semiconductor Laser"]

### [Text] Abstract

A novel hybrid surface-emitting semiconductor laser has been successfully developed. It consists of an array of end-emitting laser diodes and an Au-coated parabolic GaAs reflector. A six-element two-dimensional laser array emitting 230 mW of pulse peak power at room temperature has been fabricated.

Key Words: surface-emitting laser diode, surface array light source, semiconductor laser, visible laser diode.

### I. Introduction

Surface-emitting semiconductor lasers can be used to construct a two-dimensional surface array light source to increase the optical power output. This array has various important applications such as in optical disks, optical parallel processing, and multichannel optical communications. Surface-emitting lasers can be divided into two categories based on the type of resonance cavity. One is the vertical resonance cavity<sup>1</sup> and the other is the horizontal resonance cavity. The advantage of the former is that it is possible to achieve stable single-longitudinal-mode (SLM) operation at a low threshold. However, it is more delicate to make and requires a high degree of accuracy. Specifically, surface-emitting lasers with a horizontal resonance cavity can be further divided into the distributed Bragg reflector (DBR) type, the distributed feedback (DFB) type,<sup>2,3</sup> the 45°-bell-angle reflection type<sup>4</sup> and the curved heterojunction resonance cavity type.<sup>5</sup> The DBR or DFB types may result in a very narrow beam in the far field. Nevertheless, significant loss occurs as light passes the reflective grating. Furthermore, the fabrication of a second-order grating is also very complicated. In the single-chip reflection type employed in the past, because the quality of the etched reflection

surface and cavity surface was usually poor, the result was light loss and divergence of the optical field. It is very hard to get vertical light emission from a curved resonance activity. Based on these characteristics, some have proposed and fabricated an array of hybrid two-dimensional surface-emitting semiconductor lasers.<sup>6</sup> Because the resonance cavity and the 45°-angle reflection mirror are made of different materials, it is possible to attain a high-quality reflective surface. In addition, it is also possible to fabricate a narrow-beam and high-output power devices based on a one-dimensional phase-locked array of laser diodes. In reference 6, Si was used as the reflective surface for the surface-emitting laser. Because Si does not have a cleavage surface, it is somewhat difficult to precisely control the etching direction  $\langle 311 \rangle$  in order to obtain a 45° reflective mirror. The present paper reports a novel two-dimensional surface-emitting semiconductor laser using GaAs as the reflective surface. It is very easy to make a parabolic reflective system with GaAs. Experimental results obtained to date show that further research and development of this new type of surface diode laser array is warranted.

## II. Experimental Study

The surface-emitting laser diode discussed above was fabricated by the following process. A trimmed GaAs wafer is welded onto a Cu heat sink. Stripes 400  $\mu\text{m}$  wide and 300  $\mu\text{m}$  apart center-to-center are photolithographically etched on the wafer. Trenches approximately 70  $\mu\text{m}$  deep are etched with a  $\text{H}_2\text{SO}_4$ -based etchant. The side surface of the trench is parabolic. Au-Zn is evaporated onto the trench before laser diodes are soldered to the trenches. A cross sectional photograph of the etched trench is shown in Figure 1 [photograph not reproduced]. The structure of the surface diode laser array is shown in Figure 2.

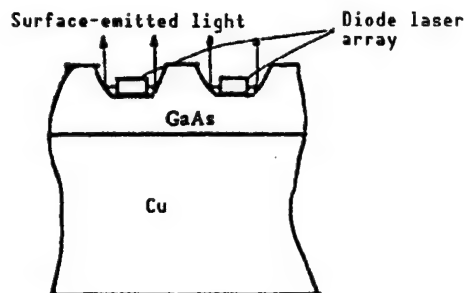


Figure 2. Structure of Surface-Emitting Laser Array

The diodes make up a terraced substrate inner-stripe visible nonphase-locked array.<sup>7</sup> On one laser chip, there are several light-emitting areas, approximately 200  $\mu\text{m}$  apart. This type of laser structure has a low threshold and good linear optical power. The wavelength is 7500–7900 Å.



### III. Experimental Results

#### (1) Reflectance

The reflectance of the etched parabolic GaAs surface and that of the Au-coated surface were determined using a setup shown in the insert in Figure 3. The results are shown in Figures 3(a) and 3(b). The reflectance of the oblique surface can be obtained from the optical power ratio of curve E to S at the same current. The curves in Figures 3(a) and 3(b) show that the reflectance of the etched GaAs surface is 80 percent if Au-coated, and 40 percent if not Au-coated. The reflectance differs quite significantly with Au-coating. This demonstrates the advantage of the separate formation of the laser diode and the reflective surface compared to the single-wafer etched surface emission. The reflectance can be greatly raised through Au-evaporation. In addition, these two sets of data are both low. One of the important reasons is that a part of the reflected light is lost. This problem will be addressed later.

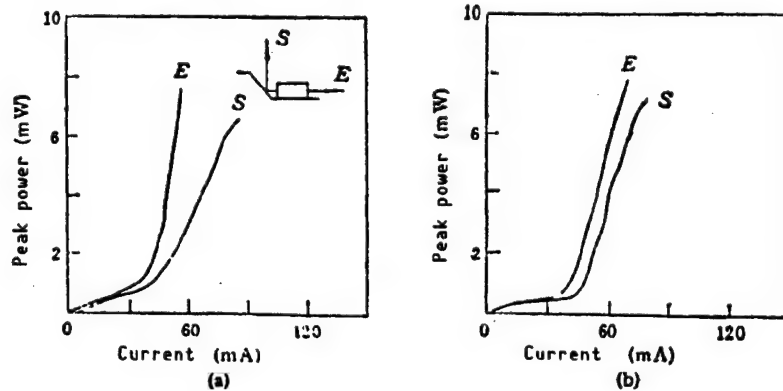


Figure 3. Optical Output Characteristic Curves of a Visible End-Emitting and Surface-Emitting Laser

- (a) shows reflection surface not Au-coated, and
- (b) is reflection angle coated with Au. E represents the P-I (power-current) curve for end emission and S represents the reflective P-I curve.

#### (2) Two-Dimensional Surface-Emitting Semiconductor Laser

A two-dimensional face-array visible surface-emitting laser has been successfully developed. Its optical characteristics and far field have been determined. The results are shown in Figures 4 and 5. The two-dimensional face array consists of two stripes with three light-emitting zones each.

The excellent linearity of the P-I curves shown in Figure 4 indicates that the end-emitting laser diode array is very uniform. This means that each emission zone has the same laser characteristics. In Figure 5, the maximum light intensity occurs at  $0^\circ$ , which is in the direction perpendicular to the substrate surface. Furthermore, the light intensity distribution covers a large range of directions. This is due to the fact that the light-emitting zones are not located at the focus of the reflective surface. Hence, some of the reflected light is lost.

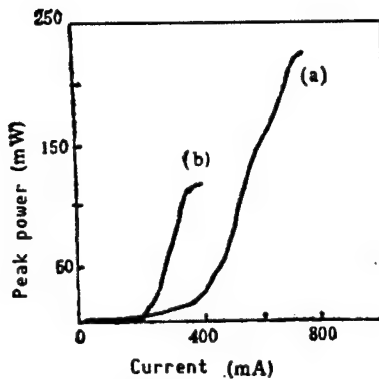


Figure 4. Optical Output Characteristic Curve for Surface-Emitting Laser

- (a) is a two-dimensional six-element array device
- (b) is the optical output of one stripe of the array in (a).

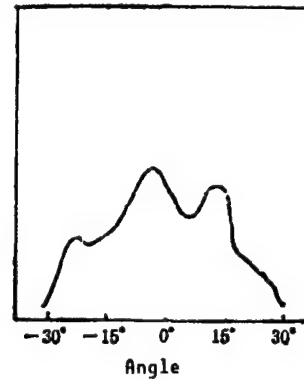


Figure 5. Far-Field Distribution of a Two-Dimensional Surface-Emitting Six-Element Laser

#### IV. Results and Discussion

We have successfully developed a two-dimensional surface-emitting visible laser array that operates in pulses at room temperature. Its maximum peak power output is 230 mW. Far-field measurement shows that reflected light is essentially perpendicular to the substrate. Based on the relatively low reflectance, some light is lost in the reflection process primarily because the end-emitting zone is close to the bottom of the reflection surface. Since the laser beam diverges, the part that diverges downward is scattered. This new surface-emitting structure can conveniently increase the number of light-emitting zones to raise the optical power output. If the depth of the trench is properly increased to reduce the distance between the active region and the heat sink to facilitate heat dissipation, this surface-emitting laser may operate continuously at room temperature. In addition, if a phase-locked laser array is used instead of an ordinary array, a narrower far-field distribution may be obtained.

Ni Jiangqiang [0242 1017 1730] was involved in some experimental work.

#### References

1. K. Iga, et al., IEEE J. QUANT. ELECTRON., Vol QF-24, 1988, p 1845.
2. N.W. Carlson, et al., APPL. PHYS LETT., Vol 50 No 19, 1987, p 1301.
3. J.M. Hammer et al., Ibid., Vol 50 No 11, 1987, p 659.
4. Z.L. Liau, et al., Ibid., Vol 46 No 2, 1985, p 115.

5. M. Ogura, et al., Ibid., Vol 50 No 12, 1987, p 707.
6. J.P. Donnelly, et al., Ibid., Vol 53 No 11, 1988, p 938.
7. Du Guotong, Zhang Xiaobo, et al., BANDAOTI XUEBAO [CHINESE JOURNAL OF SEMICONDUCTORS], Vol 11 No 4, 1990 [translated in full elsewhere in this special issue].

## Characteristics of GaAs/GaAlAs CCTS Bistable Laser

90FE0172A Beijing BANDAOTI XUEBAO [CHINESE JOURNAL OF SEMICONDUCTORS] in Chinese Vol 11 No 1, Jan 90 (MS Received 30 Dec 88) pp 28-34

[Article by Wang Qiming [3769 0796 2494], Wu Ronghan [0702 2837 3352], Zhao Jianhe [6392 1696 0735], Liu Wenxu [0491 2429 2485], and Zhang Quansheng [1728 2938 3932] of the Institute of Semiconductors of the Chinese Academy of Sciences, Beijing: "Experimental Study of Steady-State and Dynamic Characteristics of a GaAs/GaAlAs Bistable Laser"]

### [Text] Abstract

This paper reports the experimental results of static and dynamic characteristics of a GaAs/GaAlAs lateral-gain waveguide confinement bistable laser diode. The L-I [output power vs. current] behavior, mode competition during switching-on, delay, relaxation oscillation, pulsation and chaos, are investigated and the results are discussed. This experiment shows that due to the presence of a saturable absorber in the cavity, the steady-state and dynamic characteristics of a CCTS (common cavity two-section) bistable laser are more complicated than those of a uniform injection laser. The relevant physics needs to be further investigated.

Key Words: semiconductor laser, optical bistability, chaos phenomenon.

### I. Introduction

With the rapid development of optoelectronics and its applications, the study of optical bistability has been receiving more and more attention in recent years. Because of its simple structure, compactness, low power consumption, high speed, high gain, multiple facility, and ease of integration, it has a bright prospect in a broad range of applications such as high-speed modulated light sources,<sup>1</sup> semiconductor ultrafast lasers,<sup>2,12</sup> optical digital amplification,<sup>3,4</sup> optical digital coding, optical information processing and optical computing.

G.J. Lasher in 1964 discussed the feasibility of using a CCTS laser to achieve optical bistability from a theoretical perspective.<sup>5</sup> Recently, a number of theoretical and experimental studies have been conducted by H. Kawaguchi,<sup>6</sup> et

al., Yariv,<sup>7</sup> et al., and Wang Qiming,<sup>8</sup> et al., on the basic characteristics of this device. Nevertheless, not much has been published on the systematic measurement of the steady-state and dynamic characteristics of such a device. After the successful development of a GaInAsP/InP common-cavity bistable laser with lateral index-of-refraction waveguide confinement,<sup>9</sup> we employed proton bombardment to create high-impedance PN junction isolation to fabricate a GaAs/GaAlAs CCTS bistable laser with stripe geometry. Continuous bistable operation at room temperature was achieved. The minimum switching-on threshold current was as low as 50 mA. A systematic study of the steady-state and dynamic characteristics of the proton-bombarded bistable laser stripe has been done experimentally under electrical injection in this work. The results are discussed. It was found that due to the presence of a saturable absorber which causes the nonuniform distribution of various parameters and due to the variation of the lateral waveguide under high injection, the characteristics of the device are much more complicated than those of a uniform injection laser. In particular, the strong nonlinear effect under high injection makes the dynamic behavior of the device complicated and interesting. It is very difficult to explain these experimental phenomena based on the one-dimensional rate equation. More rigorous theoretical work needs to be done.

## II. Device Structure

Usually, it is desirable to have good electrical isolation between the gain area and absorber area on a chip prepared by liquid phase epitaxy. Moreover, the chip should have a low series resistance, thermal resistance, and a perfect-index-of-refraction waveguide parallel to the p-n junction. Proton bombardment was used to form the stripe geometry, approximately  $8\ \mu\text{m}$  in width. The depth of proton bombardment should not enter the active region.

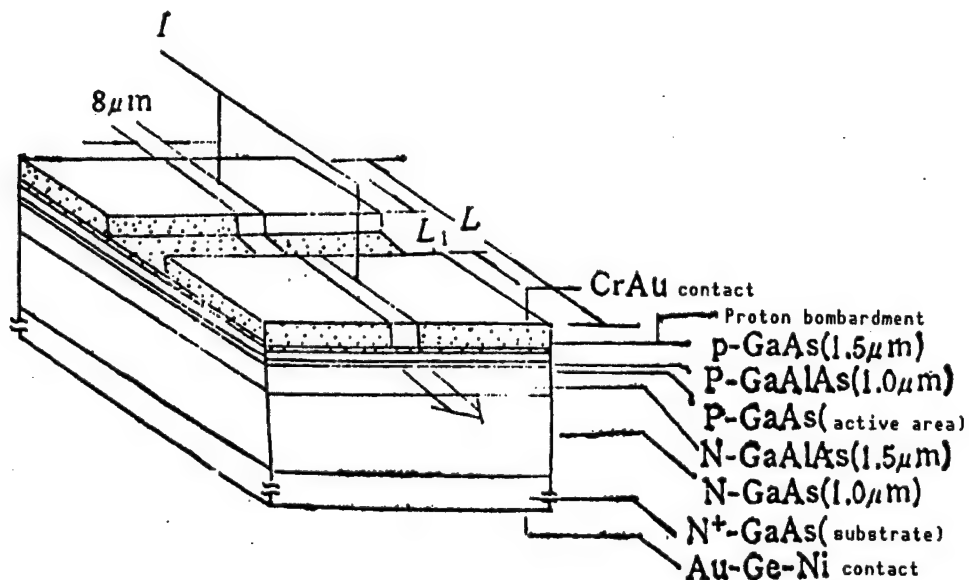


Figure 1. GaAs/GaAlAs CCTS DH Laser Structure

As seen in Figure 1, the gain area of the laser consists of two symmetric parts. A 25-50- $\mu\text{m}$  long etched trench in between is the absorbing area. The laser cavity is about 300  $\mu\text{m}$  long and the isolation resistance between the two gain areas is greater than 10 k $\Omega$ . The device was fabricated by an inverted technique and can operate with two or three terminals.

### III. Experimental Results and Discussion

#### 1. Steady-State Characteristics

##### (1) Direct-current L-I curve

The device was able to operate continuously at room temperature. The lowest switch-on lasing threshold current is 50 mA. Figure 2 shows two L-I characteristic curves for continuous operation at room temperature. Figure 2(a) shows a linear relationship between light output and injection current and Figure 2(b) shows a very gradual change in light output as a function of injection current, indicative of nonlinear saturation.

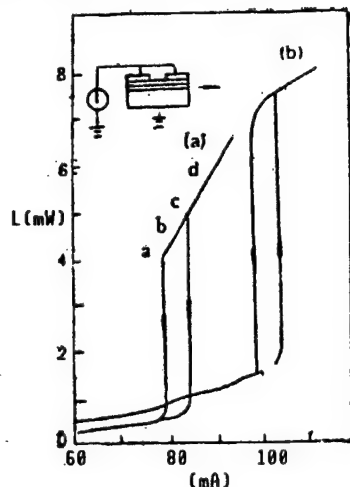


Figure 2. Two Typical L-I Curves

With regard to the near saturation of light output, one possible explanation is related to the lateral-gain waveguide. If photon bombardment is relatively shallow, the gain is close to saturation near the center of the stripe electrode. As injection current increases, the original gain distribution changes. A larger fraction of current leaks to the low gain zone and loss zone to lower the external quantum efficiency. The optical output in the switch-on mode is nearly saturated. Next, the deterioration of its thermal characteristics would also lower its external differential efficiency. However, the latter was proven not to be the primary factor by a low-frequency pulse bistability experiment.

##### (2) Pulsing bistability and switching characteristics

In order to avoid thermal effects, a step electrical pulse switch-on device, as shown in Figure 3 [photograph not reproduced], was used. A rectangular

low-frequency wide pulse ( $<1$  KC) serves as the bias. An add-on small narrow pulse switched the device from off to on and kept it on until the end of the wide pulse. By properly adjusting the bias current, it is possible to minimize the energy required to switch on the device.

### (3) Time resolution spectrum

We used low-frequency rectangular pulse injection ( $\mu\text{s}$ -level) and time-resolution spectroscopy to study the mode competition characteristics at different time intervals when the device was switched on. The spectrum measurement system is shown in Figure 4; the system's spectral resolution is approximately  $3 \text{ \AA}$ . The sampling gate width of the BOXCAR average is  $5 \text{ ns}$ . A high-speed oscilloscope was used to monitor the injected electrical wave form and optical output wave form. The spectral distribution from the sampling gate was recorded by an X-Y recorder.

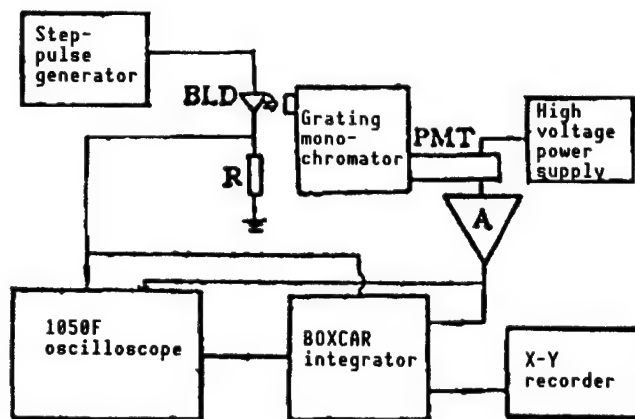


Figure 4. Schematic Diagram of Time Resolution Spectrum of the Bistable Laser

Figure 5 shows the spectra taken at various intervals after a rectangular current pulse was injected. Near the switch-on point, there are several modes of output. As several  $\mu\text{s}$  went by, only the primary mode remained and the output was enhanced. The experimental result on the intense mode competition near the switch-on point is consistent with the theoretical analysis using multi-mode rate equations.<sup>10</sup> This also indicates that the saturable absorber in the cavity has a stronger suppression effect on the peripheral modes than that in a uniform laser. It is difficult to obtain a single longitudinal mode output from a conventional  $8\text{-}\mu\text{m}$  wide photon bombarded laser with uniform injection.

The effect of temperature field distribution on the spectrum due to nonuniform injection was studied by time-resolved spectroscopy. Rectangular electrical pulses were injected at a known low frequency. Time domains with more apparent temperature variation were scanned by aiming the sampling gate at them (starting approximately from switch-on time). Spectra were recorded at  $1\text{-}\mu\text{s}$  intervals to obtain the time-resolved spectrum that describes the temperature variation, as shown in Figure 6. Qualitatively from this gradually varying

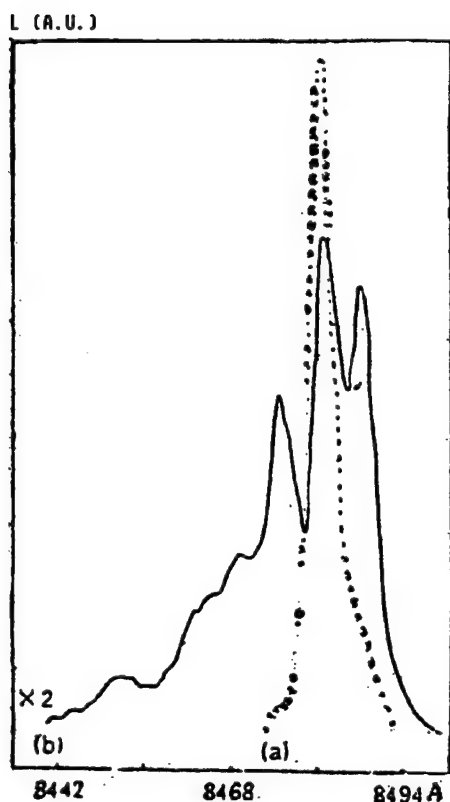


Figure 5. Time-Resolved Spectrum of Mode Competition During Switch-On

- (a) Steady-state
- (b) Upon excitation under rectangular pulse bias

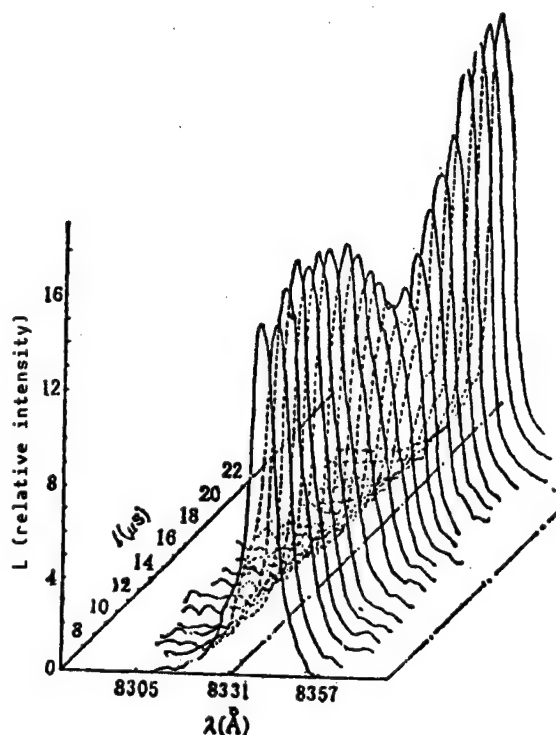


Figure 6. Time-Resolved Spectrum Showing Temperature Characteristics

process we can see that it is a competition between two main modes. As time goes by, the laser spectrum slowly changes from a shorter-wavelength single-mode output to a longer-wavelength single-mode output. However, during the transition from one peak to another, the total light intensity does not vary. When the two peaks are essentially comparable, the spectral line is the widest. After it is shifted to the longer wavelength, the mode is stable and the spectral line becomes the narrowest.

This wavelength shift might be due to the pressure of a larger temperature gradient in the resonance cavity as a result of current injection. When the temperature field stabilizes, the optical gain varies. As a result, the emission spectrum of the device also varies and shifts toward a longer wavelength. In a bistable laser, due to nonuniform injection, the temperature dependence of the spectrum should be more apparent than that of a uniform injection laser.



## 2. Dynamic Characteristics

The CCTS bistable laser includes a Q-switch function. Its instantaneous behavior is quite different from that of a conventional uniform injection laser. It has a series of complicated instantaneous behavioral responses. Due to the presence of a saturable absorber in the cavity, the loss inside the cavity increases and the carrier storage process is lengthened. Hence, under the condition of zero dc bias and pulse triggering from zero, the switching on delay might be considerably longer (even by several orders of magnitude) than that of a conventional uniform injection laser. The span of the bistable zone, which is an indication of the intensity of the Q-switch, directly affects the frequency of relaxation oscillation. It is made significantly smaller ( $<1$  GC) and the decay constant becomes larger. Initially, the spacing between oscillations increases. The first peak of relaxation oscillation shows the effect of pulse compression and its trailing edge goes down to zero. In the injection range higher than that for relaxation oscillation, the photo density and the carrier concentration in the gain and absorption area interact with each other. When a specific synchronous condition is met, sustained Q-switching was found and equal-amplitude light output was observed. As injection current continued to increase, due to various strong nonlinear effects and mutual coupling of cyclic functions, pulses were found to branch off periodically and a chaos phenomenon was observed.

### (1) Time delay

For a two-terminal device triggered by a single rectangular pulse without any dc bias, the longest time delay could be several dozen nanoseconds. For a three-terminal device, it could be as long as several hundred nanoseconds. However, for a switching laser with very small bistable width, the effective extrapolated time-delay constant is 8-9 nanoseconds, which is slightly longer than that for a conventional uniform injection laser.<sup>11</sup>

### (2) Relaxation oscillation

Relaxation oscillation occurs in a current range which is close to and slightly higher than the threshold. Due to the strong Q-switching effect, its oscillation frequency is lower than that of a uniform injection laser. With respect to different decay characteristics, it corresponds to two typical steady-state L-I curves. Normally, relaxation oscillation behaves nearly the same as in a conventional uniform laser. However, in the relaxation oscillation corresponding to nonlinear saturation and its associated L-I behavior, the trailing edge after the first oscillation peak always goes down to zero. Using this type of relaxation oscillation and a biased electrical pulse capture technique, it is relatively easy to obtain an ultrafast pulse with a FWHM [full width half maximum] of approximately 10 ps. This ultrafast light pulse will be discussed in a separate paper.<sup>12</sup>

### (3) Chaotic transformation of self-sustained pulsation

There are several papers discussing the instability of a bistable laser.<sup>6,10</sup> However, the focus of most theoretical analyses (one-dimensional rate

equation) and experimental results is placed on loss of bistability. Our device showed bistability, self-pulsation, and time chaos over different current-injection ranges. It is hard to use a simple one-dimensional rate equation to satisfactorily explain these experimental phenomena. It is necessary to consider the effect of lateral confinement, coupling of various periodic functions and strong nonlinear effects due to factors such as gain and index of refraction. Results of such a theoretical analysis will be published in the future.

The authors wish to thank other comrades in the fabrication line of the optoelectronics laboratory and the optical bistability group for their assistance and Professor Guo Changzhi [6753 7022 1807], president of Beijing University, for the beneficial discussion.

### References

1. D.Z. Zhang, et al., IEEE J. QUANTUM ELECTRONICS, Vol QE-19, 1983, p 145.
2. H. Ito and N. Ondern, ELECTRONICS LETTERS, Vol 17, 1981, p 15.
3. Wang Qiming, Wu Ronghan, Li Jianmeng [2621 1696 5536], and Wu Hong [0702 3163], BANDAOTI XUEBAO [CHINESE JOURNAL OF SEMICONDUCTORS], Vol 9, 1988, p 109.
4. U. Ohlander, P. Blixtand, and O. Sahlen, APPL. PHYS. LETT., Vol 53, 1988, p 1227.
5. G.J. Lasher, SOLID STATE ELECTRONICS, Vol 7, 1964, p 707.
6. H. Kawaguchi, IEEE PROC. Part I, Vol 129, 1982, p 141.
7. J. Katz, S. Margalit, C. Harder, D. Wilt, and A. Yariv, IEEE J. QUANTUM ELECTRONICS, Vol QE-7, 1981, p 4.
8. For example, Wang Qiming, et al., TONGXIN XUEBAO [JOURNAL OF CHINA INSTITUTE OF COMMUNICATIONS], Vol 6, 1985, p 65; WULI XUEBAO [ACTA PHYSICA SINICA], Vol 35, 1986, p 1095.
9. Li Jianmeng, Peng Huaide [1756 2037 1795], Wang Qiming, BANDAOTI XUEBAO [CHINESE JOURNAL OF SEMICONDUCTORS], Vol 8, 1987, p 222.
10. Wang Shouwu, Wang Qiming, and Ling Shiming, IEEE J. QUANTUM ELECTRONICS, Vol QE-23, 1987, p 1033.
11. Zhang Cunshan [1728 1317 0810] and Xie Jingtao [6200 0079 3447], BANDAOTI XUEBAO [CHINESE JOURNAL OF SEMICONDUCTORS], Vol 9, 1988, p 113.
12. Wang Qiming, Li Wenxu, Zhao Jianhe, and Wu Ronghan, 11th IEEE International Semiconductor Laser Conference, Boston, U.S.A., 1989, p 134.

## Single-Lobe Phase-Locked TCSIS Semiconductor Laser Array

90FE0172B Beijing BANDAOTI XUEBAO [CHINESE JOURNAL OF SEMICONDUCTORS] in Chinese Vol 11 No 1, Jan 90 (MS Received 17 Mar 89, revised 29 Aug 89) pp 77-79

[Article by Zhao Fanghai [6392 2455 3189], Du Guotong [2629 0948 0681], Zhang Xiaobo [1728 0879 3134], and Gao Dingsan [7559 7844 0006] of the Department of Electronic Science, Jilin University, Changchun: "Single-Lobe Phase-Locked Trapezoidal Channel Substrate Inner-Stripe Semiconductor Laser Array"]

### [Text] Abstract

A novel trapezoidal-channel-substrate inner-stripe (TCSIS) semiconductor laser array, which can be fabricated by a one-step liquid phase epitaxy (LPE) technique, is designed and developed. The single-face power output of a continuous-wave (CW) device and that of a pulsed device are greater than 76 mW and 675 mW, respectively. The far-field single-lobe half-width angle is only  $2.4^\circ$ .

Key Words: trapezoidal channel substrate, inner stripe, one-step liquid phase epitaxy, array.

### I. Design Concept

Numerous types of phase-locked semiconductor laser arrays have been designed and developed. Nevertheless, they can all be divided into two basic categories based on the waveguide mechanism; i.e., gain-waveguide array and (forward) index-of-refraction waveguide array. It has been demonstrated both experimentally and theoretically that a gain-waveguide array has higher output power. However, double peaks may appear in the far field<sup>1</sup> which make practical applications difficult. Compared to a gain-waveguide array, it is easier for an index-of-refraction array to have a single peak in the far field. However, the lobe width is wider and the power is lower. In order to overcome the shortcomings of these two types of phase-locked semiconductor laser arrays, a novel array structure, the TCSIS phase-locked semiconductor laser array, has been designed based on existing experimental conditions. It has both forward and reverse index-of-refraction waveguide structure and can easily be prepared using a re-melting technique with one-step LPE.

## II. Device Structure and Fabrication

Figure 1 shows the cross section of a triple TCSIS semiconductor laser array.

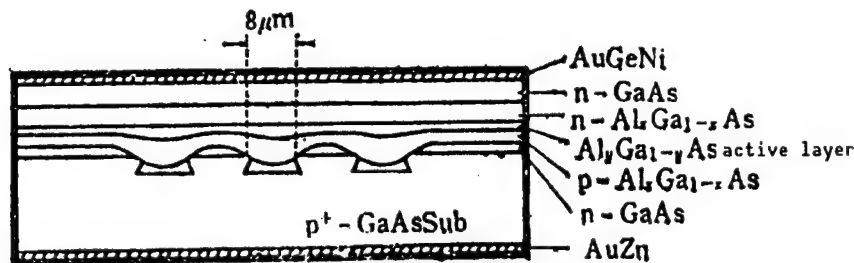


Figure 1. Cross Section of the Device

The device was fabricated by taking advantage of the growth mechanism of LPE on a nonplanar substrate. Through rigorous control of factors such as the initial supercooling temperature of the growth solution, initial growth temperature and rate of temperature drop, the growth solution only re-melts the sharp corners at the channel shoulder during the process of growing the first current blockage layer to naturally form an inner current-limiting channel with an approximate effective width of  $1\mu\text{m}$ . Four more layers are grown on top of it. Because the inner current channel is naturally formed and is automatically aligned with the waveguide, there is no need for masking, photolithography, and Zn diffusion after epitaxy. Direct large-area ohmic contact can also be made. Thus, the detrimental effects on the quality of the crystal due to these processes can be avoided.

Furthermore, the lateral thickness variation during LPE on a nonplanar substrate makes the effective index of refraction increase gradually on one side of the light-emitting zone. This forms a reverse index-of-refraction waveguide. The optical field is coupled by leaky waves. The coupling is strong, but mode limitation is weak. On the other side, however, the index-of-refraction gradually decreases, forming a forward index-of-refraction waveguide. The optical field is coupled by evanescent field coupling, which is weak; however, the mode limitation is strong. As far as an individual laser is concerned, it is a classical semi-leaky wave waveguide laser. Based on literature,<sup>2</sup> this waveguide laser can easily go into fundamental mode oscillation. To this end, we believe that this structure, to some extent, absorbs the advantages of both the gain waveguide and index-of-refraction waveguide arrays and partially compensates for their shortcomings. Of course, this point needs to be proved by further theoretical analysis. Experimentally, we have fabricated a fundamental supermode Third Research Laboratory device with excellent single-lobe far-field output.

## III. Experimental Results

The lowest threshold current of the triple TCSIS laser array we have fabricated to date is 170 mA in CW mode at room temperature ( $21^\circ\text{C}$ ). The maximum single-face dc light output power was measured at 76 mW. The peak light output power for a single pulse (200 ns, 5 kHz) is greater than 675 mW. The light output power vs. current curve is shown in Figure 2.

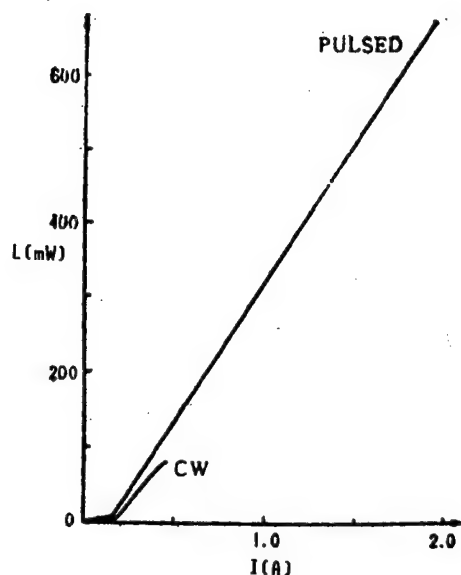


Figure 2. Light Output Power vs. Current

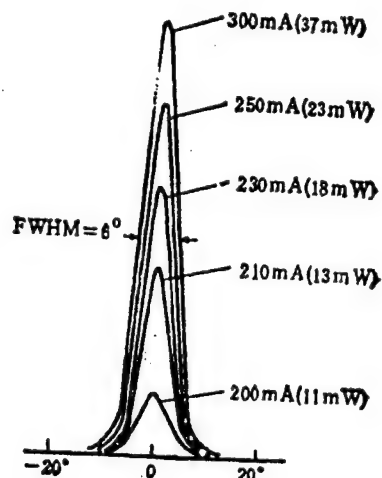


Figure 3. Far-Field Light Intensity Distribution in Continuous-Wave Operation

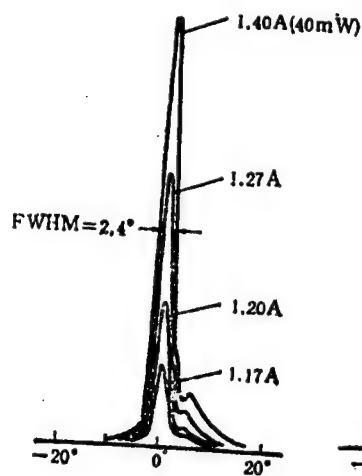


Figure 4. Far-Field Light Intensity Distribution in Pulsed Operation

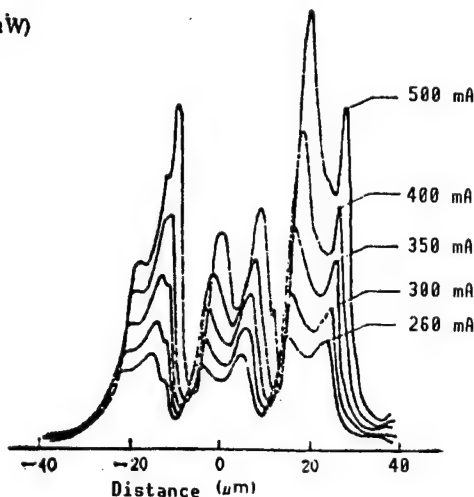


Figure 5. Near-Field Light Intensity Distribution in Continuous-Wave Operation

#### IV. Conclusions

Experimentally, it was demonstrated that the TCSIS phase-locked semiconductor laser array with both forward and reverse index-of-refraction waveguides that we designed and developed was easy to fabricate and performed very well. The triple-channel, six-laser device thus fabricated is an excellent single-lobe fundamental supermode oscillation device with a lowest dc threshold current of 170 mA, single-face CW power output greater than 76 mW, pulsed peak power greater than 675 mW, and far-field half width of  $2.4^\circ$ .

### References

1. Y. Twu, S. Wang, J.R. Whinery, and A. Dinens, IEEE J. QUANTUM ELECTRONICS, Vol QE-23, 1987, p 788.
2. D. Botez, Ibid., Vol QE-17, 1981, p 2290.

## GaAs/GaAlAs SQW Electroabsorption and Light Modulation

90FE0172C Beijing BANDAOTI XUEBAO [CHINESE JOURNAL OF SEMICONDUCTORS] in Chinese Vol 11 No 3, Mar 90 (MS Received 26 May 89) pp 202-209

[Article by Zhu Longde [2621 7893 1795], Xiong Feike [3574 7378 0344], and Wang Qiming of the Institute of Semiconductors of the Chinese Academy of Sciences, Beijing, and Chen Zhengdao [7115 2973 6275], Xie Yuanlin [6200 5373 2651] and Gu Shijie [7357 0013 2638] of the Institute of Physics of the Chinese Academy of Sciences, Beijing: "GaAs/GaAlAs SQW Electroabsorption and Light Modulation"]

### [Text] Abstract

GaAs/GaAlAs separate confinement single quantum well (SQW) single-mode ridge-waveguide electroabsorption optical modulators were fabricated and studied. The maximum modulation depth (on/off ratio) for TE polarized light at 8650 Å is 29.7 dB with a 100 Å-wide quantum well, 700-μm long device. The absorption portion of insertion loss is 3 dB. The maximum modulation depth for TM polarized light is 28.5 dB. A 15 dB on/off ratio can be achieved with 2 V. Photocurrent spectra exhibited a 600 Å red shift of the absorption edge when the bias voltage varied from +0.5 V to -7 V, corresponding to a shift of 96 meV in the resonance absorption peak of the exciton in the quantum well at room temperature. For the first time, the presence, enhancement, and shift of the exciton-resonance absorption line between electrons in the second quantum level in the conduction band and holes in the first level have been observed.

**Key Words:** GaAs/GaAlAs single quantum well, single-mode ridge-waveguide modulator, quantum confined Stark effect, modulation depth (on/off ratio), forbidden transition.

### 1. Introduction

Since semiconductor quantum well and superlattice structures became known, one of the physical phenomena discovered is the presence of the room-temperature exciton.<sup>1</sup> This is due to an increase of the exciton combination energy when the dimension of the quantum well is less than the Bohr diameter (~300 Å) of a three-dimensional exciton.<sup>2,3</sup> Because of the step-wise energy state density distribution in the quantum well,<sup>4</sup> as well as the presence of a

room-temperature exciton resonance absorption peak,<sup>1-3</sup> The absorption spectra of quantum well and superlattice materials have very steep absorption edges. When an electric field is applied to the semiconductor, the absorption edge would expand (Franz-Keldish effect).<sup>5</sup> When an electric field perpendicular to the layers is applied to a quantum well material, a red shift of the exciton absorption edge occurs.<sup>6</sup> This red shift is quite significant, as high as 20 meV/105V/cm.<sup>7</sup> This phenomenon, the quantum confined Stark effect (QCSE),<sup>7,8</sup> primarily consists of two parts—quantum energy-level shift caused by the electric field and reduction of exciton binding energy.<sup>7,8</sup> Quantitatively, the former is the main factor. This room-temperature exciton Stark effect in the quantum well has very promising applications in devices such as electroabsorption optical modulators and light switches,<sup>9,10</sup> as well as self-electrooptic effect devices (SEEDs), such as optically bistable devices.<sup>11</sup> In order to raise the mutual interaction volume of the transmission-mode optical field and the electric field, most published studies have used multiple quantum well (MQW) and superlattice materials.<sup>9</sup>

A GaAs/GaAlAs separate-confinement SQW laser has advantages such as low threshold current and insensitivity of threshold current to temperature.<sup>13</sup> Although the electroabsorption and modulation characteristics of the GaAs/GaAlAs SQW double-heterojunction (DH) have been reported in the literature,<sup>14</sup> a detailed study on a separate-confinement SQW modulator has not been reported. Considering the feasibility of integrating a low-threshold laser and optical modulator of similar structure,<sup>10</sup> and considering the feasibility of using such a modulator in a low-loss logic switch array, we have investigated the electroabsorption and electrooptical modulation of the GaAs/GaAlAs separate-confinement SQW optical modulator.

## II. Fabrication of GaAs/GaAlAs Separate-Confinement SQW Optical Modulator

The GaAs/GaAlAs separate-confinement SQW structure was prepared by MOCVD [metal-organic chemical vapor deposition]. The width of the quantum wells is 100 Å. The undoped quantum well is sandwiched between two 0.2- $\mu\text{m}$  thick undoped waveguides with a graded index of refraction. The aluminum content varied linearly from 0.2 at the edge of the well to 0.5 at the edge of the confinement layer. The confinement layers are two 1.5- $\mu\text{m}$  thick GaAlAs layers with an 0.5 aluminum content. Such a structure meets the requirement to cut off higher-order modes. Hence, only the fundamental transverse mode exists perpendicular to the surface. Two 5- $\mu\text{m}$  wide channels were etched on the surface along the [011] direction to form a 2.5~4.0- $\mu\text{m}$  wide mesa waveguide in between. Since the channels were critically etched to within 0.2  $\mu\text{m}$  of the active layer, the effective lateral index or refraction distribution creates the light confinement to form a mesa light waveguide in the fundamental mode. A top view micrograph of the waveguide modulator is shown in Figure 1 [photograph not reproduced]. The lateral two-dimensional fundamental mode of this modulator was confirmed experimentally by the fact that the near-field image of the transmitted light has only a single light spot. The wafer was sliced into 700  $\mu\text{m}$  or 300  $\mu\text{m}$  strips and then cut into 300- $\mu\text{m}$  wide chips. It was sintered with the P side facing up on a copper heat sink. The width of the heat sink is comparable to that of the length of the modulator to facilitate the coupled input and output of light. Due to the diffusion of Zn in the P



type confinement layer during the growth process, the p-n junction was shifted to the edge of the quantum well. As for the V-I curve, the forward injection voltage is 1.5 volts. The reverse breakdown voltage of the device is 14 volts. Prior to breakdown, the dark current is less than the 1- $\mu$ A current detection sensitivity.

### III. Photocurrent vs. Bias Voltage for GaAs/GaAlAs Separate-Confinement SQW Optical Modulator

The modulator is actually a PIN [photo] diode. The quantum well is in the depletion layer in zone I. A bias voltage produces a specific electric field in the quantum well. The dependence of the absorption characteristics of the quantum well upon the electric field can be determined by measuring the photocurrent spectra of the PIN diode as a function of bias. The light from a high-intensity tungsten iodine lamp was passed through a single-grating spectrograph and was focused on the waveguide modulator using a 40x lens. The optical signal was recorded on an X-Y recorder after phase-locked amplification. The load resistance is 47 $\Omega$ , which is far less than the reverse dynamic resistance ( $>>10^6\Omega$ ). Some spectral resolution was sacrificed (several dozen angstroms) to compensate for the lack of sufficient incident light intensity.

Figures 2(a) and 2(b) show the photocurrent vs. bias plots for the TE and TM mode, respectively. Within the bias range of +0.5 V to -7 V, the collection efficiency of light-induced carriers is 1. In addition, within the wavelength range shown, the spectrum of the light source varied very slowly. Therefore, the photocurrent spectrum is a direct reflection of the light absorption spectrum. We can see that the absorption edge is very steep. The photocurrent dropped from its peak at 0.9 to 0.1 in less than 200 Å. The steep decline varied very little up to a bias of -7 V. Exciton resonance peaks on absorption edges were clearly visible. Based on selection rules, the absorption peak in the TM spectrum ought to be caused by light-hole exciton (CB1-lh1), while that in the TE spectrum should be caused by both light- and heavy-hole excitons. The exciton absorption peak is more prominent in a TM spectrum than that in a TE spectrum. Further, the energy is also higher (especially between +0.5 V and -1 V). This is in agreement with the above selection rules. Since the spectral resolution is poor in our measurement and the result is the mean over the entire length of the waveguide, the heavy- and light-hole exciton peaks were not resolved in Figure 2(a). Instead, they appeared as broad absorption peaks. The absorption edge shifts significantly with applied electric field: 600 Å as the bias varied from +0.5 V to -7 V. On an average, it shifts 84 Å/V. Figure 3 shows how the absorption peak energy shifted with bias. It moved 96 meV, or an average of 13 meV/V. Under low bias, the TM absorption peak energy is higher and it shifts more. It should be pointed out that because of the presence of an internal field the peak still shifts with a +0.5 V bias. We will show later that the quantum well becomes a square and the absorption edge tops moving well after a bias of +1.0 V is applied. In the photocurrent spectra, the TE-polarized photocurrent is 20 percent higher than the TM-polarized photocurrent. However, the intensity of a TE-polarized absorption peak declines faster than that of a TM-polarized absorption peak. That is, the overlapping integral of the transition matrix-element electron-wave function and hole-wave function declines very fast with the electric field. Based on

Figure 2, the operating band of the modulator fabricated with the 100 Å quantum well material is 8650~8950 Å within +0.5 V to -7 V. In this 300 Å range, the extinction ratio deterioration is less than 5 percent. The switching voltage is 2 volts.

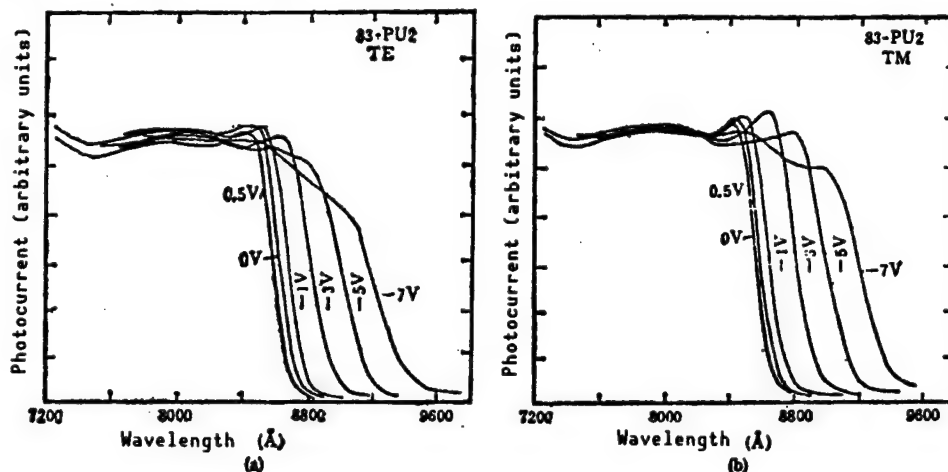


Figure 2. PIN Diode Photocurrent Spectra vs. Bias Voltage  
(a) TE polarization; (b) TM polarization

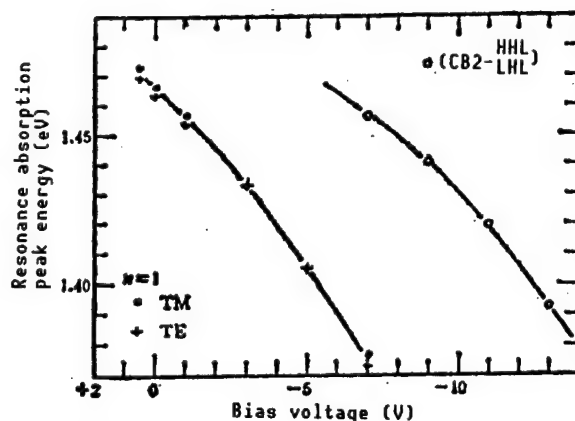


Figure 3. Room-Temperature Exciton Resonance Peak Energy vs. Diode Bias Voltage  
+: ( $CB1-hh1$ ) exciton peak; •: ( $CB1-lh1$ ) exciton peak;  
o: ( $CB2-hh1$ ) exciton peak

The absorption peak edge photocurrent spectra of the modulator over a wider bias range is shown in Figure 4. From +0.5 V to -9 V, the short-wavelength edge photocurrent essentially remained unchanged. It fell when the positive bias is greater than +0.7 V. This is because light-induced carriers cannot be swept out, resulting in a reduction of collection efficiency. When the negative bias is greater than -10 V, the short-wavelength photocurrent increases because the electric field is close to breakdown, and micro-breakdown in the P-N junction occurs. The most interesting thing in this figure is the

appearance of another absorption peak when the negative bias is greater than  $-5$  V. After this absorption peak appears, its intensity increases with increasing bias. Its energy also shifts with bias, as shown in Figure 3. This absorption peak is attributed to the exciton resonance peak formed between electrons in the second quantum level in the conduction band and hole in the first energy level in the valence band. This transition is forbidden in a symmetric quantum well. Therefore, the transition probability of a ground-state exciton is high at low bias. When the electric field goes higher, because of larger spatial separation between electrons and holes, the transition probability for a ground-state exciton declines. The overlap integral between states of different symmetry, where transition was forbidden, is no longer zero. Instead, it gets larger with increasing electric field. The wave function of the high-energy electron state does not vary much with the

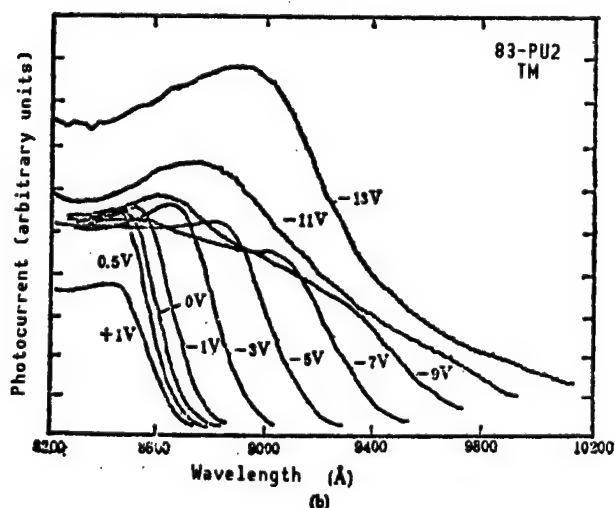
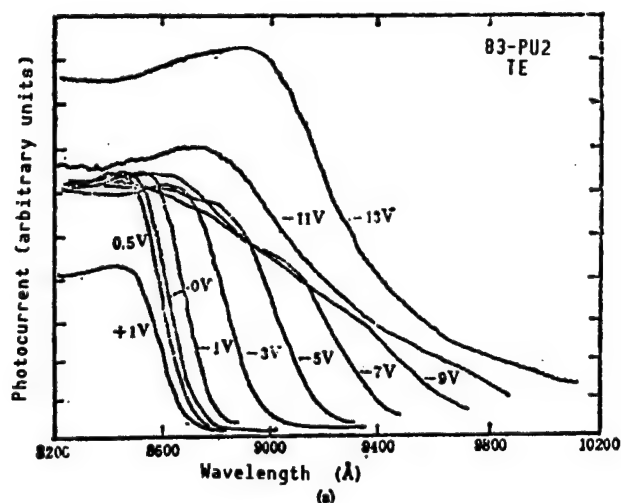


Figure 4. Photocurrent Spectra vs. External Bias of the Modulator From  $+1$  V to  $-13$  V  
(a) TE polarization; (b) TM polarization

electric field, but the low-energy hole wave function in the triangular well varies quite a great deal with the electric field, thus causing the appearance and enhancement of this absorption peak. We believe that the appearance, enhancement and shift of this peak was observed for the first time, probably because we were able to apply a very strong electric field ( $\sim 13$  V) to the (single-well) specimen.

#### IV. Electroabsorption Light Modulation Experiment and Device Modulation Characteristics

The separate-confinement structure has excellent light-confinement characteristics. However, the light-confinement factor of an SQW is low,  $\Gamma = 0.03$ . Therefore, by properly increasing the length of the device it would be possible to raise the electroabsorption attenuation of the light in the transmission mode at peak absorption in order to increase the modulation depth. In addition, by properly selecting the wavelength based on the electroabsorption spectrum of the specimen, it is possible to still keep the on loss of the modulator low and also lower the modulation voltage and bias voltage as well. Since the modulator to be measured has a single-transverse-mode waveguide, it is best to use a well-collimated high-power light source to ensure the accuracy of the experiment. The light modulation experiment setup is shown in Figure 5. The light source is an argon-ion-laser-pumped LDS821 tunable dye laser. The tunable output wavelength range is 8300-8700 Å. A 40x microscope object lens was used to focus the light on the sliced face of the modulator. The light output from the waveguide was coupled to a single-mode or multimode optical fiber and received by an S-1 photomultiplier tube and a phase-locked amplifier. When adjusting input coupling, the modulator may serve as a light detector to maximize the photocurrent with the three-dimensional modulator. The coupling between the modulator and the optical fiber may be done in two ways. One is to use the modulator as a laser or a light emitter. The other is to apply a modulation voltage on top of CW light transmission at the operating wavelength and measure the modulated output light. The goal is to maximize the signal; i.e., using the light modulation property of the device for coupling.

Figure 6 shows the normalized transmitted power as a function of dc bias in the TE and TM mode for a 700- $\mu\text{m}$  long single-transverse-mode modulator at 8550, 8600, and 8650 Å. Since the absorption characteristics of the quantum-well waveguide differ in TE and TM polarized mode, the measured static modulation curves are different for the two types of polarized light. The TE modulation curve drops rapidly with increasing reverse bias. At 8550 Å, TE light modulation has deteriorated because the wavelength is the limiting wavelength of the exciton absorption edge. As far as TE polarization is concerned, at 8550 Å insertion absorption loss is significant. Table 1 shows the maximum modulation depths (on/off ratios), calculated from the curves, as a function of wavelength and polarization. It is evident that when wavelength is properly increased, because absorption is reduced during the on state, maximum modulation depth is raised. At 8650 Å, on/off ratios of the 29.7 dB (TE) and 28.5 dB (TM) were obtained. It is also possible to see from the modulation curve that a 2 V bias could produce a modulation depth of over 15 dB at 8600 Å. When the wavelength is 8600 Å, a 300- $\mu\text{m}$  long modulator was found to have a 15 dB on/off ratio with TE polarization and 22 dB with TM polarization.

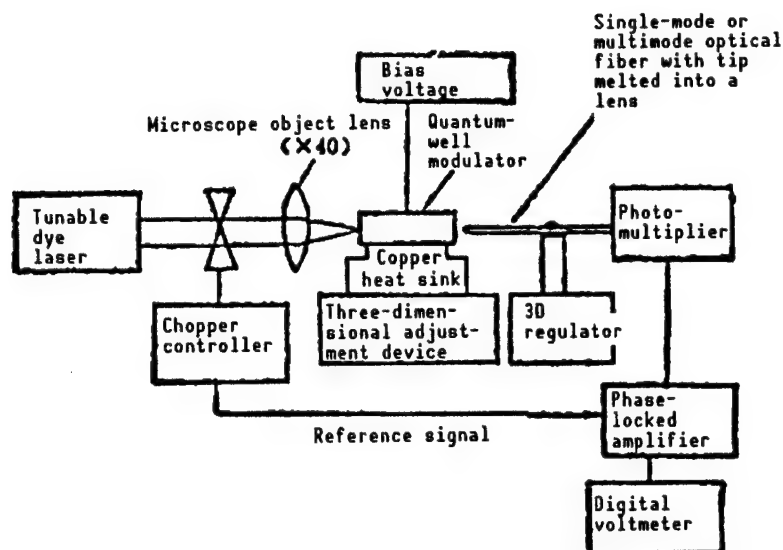


Figure 5. Experimental Setup for Electroabsorption Light Modulation

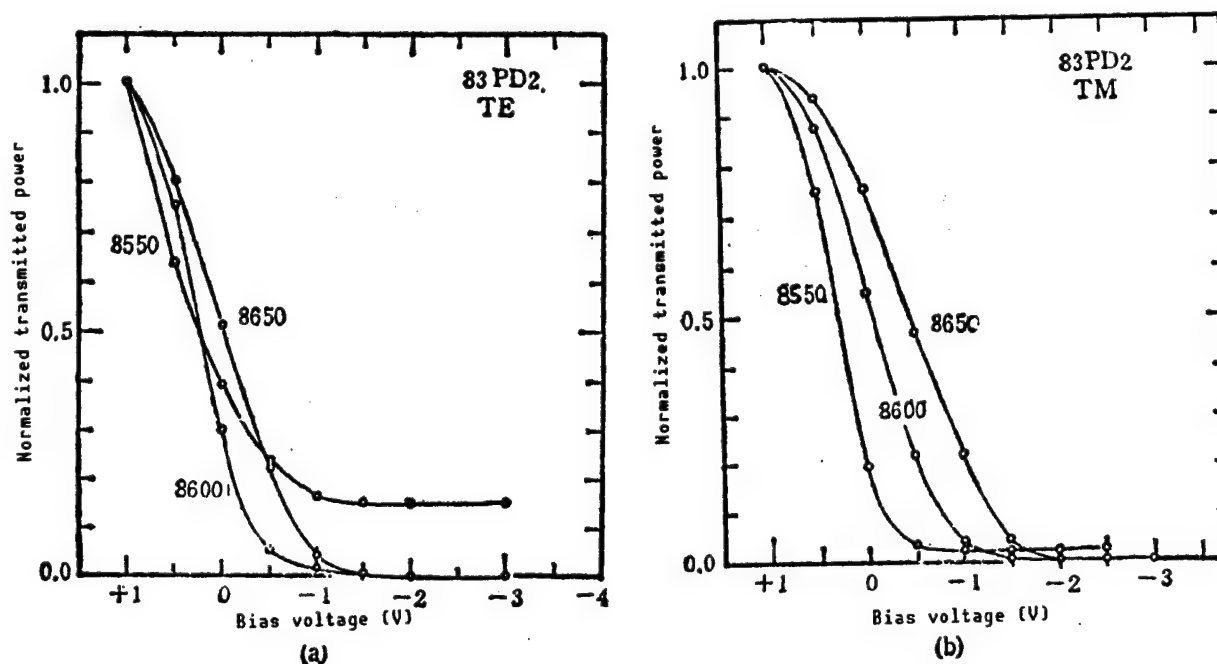


Figure 6. Normalized Transmitted Power vs. Bias Curves for a GaAs/GaAlAs Separate-Confinement SQW Single-Mode Waveguide Electroabsorption Light Modulator  
(a) TE polarization; (b) TM polarization

The limiting insertion loss of the modulator is determined by the absorption loss during on time and the scattering loss. If the steepness of the hetero-junction interface is of the order of single-atom-layer level and the lateral confinement structure of the waveguide is perfect, such as a mesa waveguide

Table 1. Maximum Modulation Depths (On/Off Ratios) of a 700- $\mu\text{m}$  Long GaAs/GaAlAs Separate Confinement 100- $\text{\AA}$  Wide SQW Single-Transverse-Mode Waveguide Modulator

Maximum modulation depth (dB)	Wavelength ( $\text{\AA}$ )	8550	8600	8650
	Polarization			
TM		18	26.3	28.5
TE		8.3	26.5	29.7

fabricated by reactive ion etching [RIE] technique, then scattering loss is very low. The limiting insertion loss is mainly determined by the absorption loss when the device is turned on. We employed the method of T.H. Wood<sup>15</sup> and determined that  $\alpha_{\min} (+1 \text{ V})L = 0.7$  at 8650  $\text{\AA}$  based on the data on photocurrent and transmitted power as a function of bias. Thus, the on-state TE-mode absorption coefficient is  $\alpha_{\min} (+1 \text{ V}) = 10 \text{ cm}^{-1}$  and the absorption coefficient at -2 V bias is  $\alpha_{\text{abs}} (-2 \text{ V}) = 75.8 \text{ cm}^{-1}$ . Therefore, the insertion loss of a 700- $\mu\text{m}$  long modulator for TE waves is 3 dB. These numbers are consistent with the fact that the device was measured to have a modulation depth of 20 dB at this bias level. Based on the above analysis, despite the fact that the light-confinement factor of SQW materials is low, because quantum-well absorption can vary by several orders of magnitude due to the QCSE, it is nevertheless possible to achieve a very low insertion loss and very high modulation depth by choosing an appropriate operating wavelength and device length.

The output light waveform, shown in Figure 7 [photograph not reproduced], was observed while a triangular wave was applied to the modulator in order to obtain an intuitive modulation curve. The triangular wave varied from +1 V to -6 V. It was observed that the shorter the wavelength the sharper the on-state (+1 V) waveform becomes because the wavelength is closer to the absorption edge. Figure 8 [photograph not reproduced] shows the oscilloscope trace of the on/off signal of the modulator. The upper part is the square-wave bias voltage and the lower part is the transmitted light signal. The wavelength is 8550  $\text{\AA}$ , bias is zero and switching voltage is +1 V to -1 V. It is obvious that complete light switching can be accomplished. When a  $\pm 0.5 \text{ V}$  sinusoidal wave was used instead of the switching pulse, the simulated modulation characteristics shown in Figure 9 [photograph not reproduced] were observed. There is very little distortion.

## V. Conclusions

The room-temperature electroabsorption and optical modulation characteristics of a GaAs/GaAlAs separate-confinement SQW mesa waveguide PIN diode have been investigated. Because the 100  $\text{\AA}$  thick quantum well is located in the zero-bias depletion layer in zone I, the internal field at zero bias is very high.

Therefore, the effective bias range for the QCSE is +1 V to -10 V. Due to the presence of the room-temperature exciton absorption peak and the step-wise energy state density in the quantum well, the absorption edge is very steep. From the position and intensity of the resonance absorption peak and the modulation curve of the device, the TM polarization absorption peak is attributed to light-hole exciton absorption and the TE polarization peak is attributed to heavy- and light-hole exciton absorption. The dependence of photoelectric resonance absorption peak upon bias can be explained by the overlap integral of the wave functions of heavy- and light-hole excitons. Since it is an SQW and there is no external electric field expanding into the quantum well, the absorption edge over the above bias range is quite significant. From +0.5 V to -7 V, the absorption edge shifted by 600 Å; correspondingly, the resonance absorption peak shifted 96 meV. The effective operating bandwidth of the modulator is 300 Å. Because it is an SQW, a high electric field may be applied. For the first time, we observed the exciton resonance absorption involving electrons in the second quantum energy level and holes in the first level. It began to appear at a -7 V bias and became stronger and shifted with the electric field. This indicates that the original selection rule is overturned because the symmetry of the wave function in the quantum well is destroyed.

The 100 Å wide quantum well GaAs/GaAlAs separate-confinement SQW mesa waveguide single-mode modulator has a maximum modulation depth of 28.5 dB with TM polarization and 29.7 dB with TE polarization at 8650 Å. The absorption portion of the TE polarized insertion loss is 3 dB. This suggests that it is less than 1 dB when the device is less than 200 μm long. The operating voltage range of the modulator is +1 V to -7 V. At the proper wavelength and bias, an on/off ratio of over 15 dB can be obtained with a 2 V switching voltage. There is a compromise between insertion loss and on/off ratio if the device length and operating wavelength are properly selected. Hence, it is possible to obtain a high modulation depth, low insertion loss, and low operating voltage electroabsorption light modulator.

The GaAs/GaAlAs separate-confinement SQW mesa waveguide structure is a successful laser structure.<sup>16</sup> It has been proven to be a good electro-absorption optical modulator and light switch. This also projects that this type of laser, amplifier, modulator, and light switch can be integrated on a single chip to be used in optical information exchange such as an optical switching logic array.

The authors wish to express their gratitude to Xie Yuli [6200 3768 7787] for her assistance in device fabrication.

#### References

1. T. Ishibashi, S. Tarucha, and H. Okamoto, Proc. Int. Symp. GaAs and Related Compounds, Inst. Phys. Conf., No 63, Japan, 1981, p 587.
2. S.W. Kirchoefer, N. Holonyak, K. Hess, D.A. Gulino, H.G. Drickamer, J.J. Coleman, and P.D. Dankus, APPL. PHYS. LETT., Vol 40, 1982, p 821.

3. D.A.B. Miller, D.S. Chemla, D.J. Eilenberger, P.W. Smith, A.C. Gossard, and W.T. Tsang, *Ibid.*, Vol 41, 1982, p 679.
4. R. Dingle, W. Wiegmann, and C.H. Henry, *PHYS. REV. LETT.*, Vol 33, 1974, p 827.
5. L.V. Keldish, *SOVIET PHYSICS-JETP*, Vol 7, 1958, p 788; W. Franz, *Z. Naturforsch.*, 13a, 1958, p 484.
6. T.H. Wood, C.A. Burrus, D.A.B. Miller, D.S. Chemla, T.C. Damen, A.C. Gossard, and W. Wiegmann, *APPL. PHYS. LETT.*, Vol 44, 1984, p 16.
7. D.A.B. Miller, D.S. Chemla, and T.C. Damen, *PHYS. REV. LETT.*, Vol 53, 1984, p 2173.
8. D.A.B. Miller, D.S. Chemla, T.C. Damen, A.C. Gossard, W. Wiegmann, T.H. Wood, and C.A. Burrus, *PHYS. REV.*, Vol B32, 1985, p 1043.
9. T.H. Wood, C.A. Burrus, D.A.B. Miller, D.S. Chemla, T.C. Damen, A.C. Gossard, and W. Wiegmann, *APPL. PHYS. LETT.*, Vol 44, 1984, p 16.
10. S. Tarucha and H. Okamoto, *Ibid.*, Vol 48, 1986, p 1.
11. D.A.B. Miller, D.S. Chemla, T.C. Damen, T.H. Wood, C.A. Burrus, A.C. Gossard, and W. Wiegmann, *IEEE J. QUANT. ELECTRON.*, Vol QE-21, 1985, p 1462.
12. K.Y. Lau, P.L. Derry, and A. Yariv, *APPL. PHYS. LETT.*, Vol 52, 1988, p 88.
13. L.D. Zhu, B.Z. Zheng, and G.A.B. Feak, *IEEE J. QUANT. ELECTRON.*, Vol AE-25, 1989, p 2007.
14. N.K. Dutta and N.A. Olsson, *ELECTRON. LETT.*, Vol 23, 1987, p 853.
15. T.H. Wood, *APPL. PHYS. LETT.*, Vol 48, 1986, p 1413.
16. L.D. Zhu, G.A.B. Feak, R.J. Davis, and J.M. Ballantyne, *IEEE J. QUANT. ELECTRON.*, Vol QE-23, 1987, p 309.



## **Bistable Laser Diode Integrated Monolithically With Photodetector**

90FE0172D Beijing BANDAOTI XUEBAO [CHINESE JOURNAL OF SEMICONDUCTORS] in Chinese Vol 11 No 3, Mar 90 (MS Received 3 Mar 89) pp 210-214

[Article by Yan Xuguang [2518 4872 0342] of Hangzhou Institute of Electronic Engineering, and Humio Inaba of the Research Institute of Electrical Communication, Tokyo University, Japan: "Characteristics of a Bistable Laser Monolithically Integrated With a Photodetector"]

### **[Text[ Abstract**

For the first time, optical bistability of single-chip integration of PD/LD (photodetector/laser diode) using light output feedback pumping has been observed. The circuit is simple and the reliability is excellent. The width of bistability can be adjusted over a large range. The steady-state behavior of this bistable laser is calculated based on the rate equations of a semiconductor diode laser. There is good agreement between experimental result and theoretical calculation.

**Key Words:** integration, bistability, semiconductor laser.

### **I. Introduction**

Because an optically bistable device can be used in optical switching, memory, amplification and optical digital data-processing systems, it is a basic element in optical communications and optical computing. Therefore, it has attracted much attention in the past decade. There are scores of devices operating with optical bistability. As a good example, A. Migus and H.M. Gibbs developed a GaAs/AlGaAs multiple quantum-well (MQW) optically bistable device with a nonlinear Fabry-Perot resonance cavity. As an optical NOR gate, the switching time is 1 picosecond at room temperature. The recovery time of the gate is only a few nanoseconds.<sup>1</sup> Furthermore, W.F. Sharfin and M. Dagenais used a semiconductor laser as a nonlinear Fabry-Perot cavity and found that the room-temperature switching time was <1 nanosecond and the required input light energy was <1 fJ [femtojoule] (i.e., <7000 photons).<sup>2</sup> This indicates that an active optically bistable device has a distinct advantage in processing very weak light signals. Although some devices have been used as optical switches experimentally, their bistability characteristics (such as width of

bistability and magnitude of the output light signal) cannot be adjusted and controlled by external optical elements or electrical circuit parameters. Therefore, these devices are far from useful in real applications.

A practical optically bistable device must have excellent stability, reliability, and reproducibility. In addition, we should be able to adjust and control the bistability range and the output light signal magnitude based on the intensity of the light pulses to be processed. In addition, the device should be simple in structure and easy to fabricate (including the ability to fabricate an array with a large number of bistable devices to facilitate parallel processing of optical signals). Of course, the response time has to be fast and the cost must be low.

One of the authors suggested earlier that a conventional laser can exhibit optical bistability using either light output feedback pumping or light output feedback loss modulation.<sup>3,4</sup> Recently, we employed the light output feedback pumping mode to observe excellent controllable optical bistability with an integrated bistable laser diode (IBILD) consisting of a laser diode and a photodetector integrated on a single chip. Its control circuit is simple; by changing the circuit parameters, the width of bistability can be controlled over a wide range. Moreover, the output light intensity can also be varied.

## II. Experimental Results

Figure 1 shows the IBILD structure and the associated electrical circuit. The IBILD is an integrated device consisting of a 1.5- $\mu\text{m}$  InGaAsP distributed feedback laser diode and a photodetector (DFB-LD/PD model SB67B-3). The threshold current of the laser diode is 55 mA. The photodetector PD and the triode transistor  $T_r$  are used in the feedback circuit. The PD can simultaneously receive the laser output from LD and the external input light signal.  $V_A$  is the power supply.  $R_1$  and  $R_2$  are used to control the current to LD and PD. The operating principle of this device can be explained as follows. When the current going through LD reaches the threshold, LD begins to resonate. A photocurrent is produced by PD after it detects the laser output from LD. This photocurrent is amplified by the triode  $T_r$  and then goes to LD to cause the pumping current of LD to rise. As a result, the output from LD intensifies. As the light output from LD intensifies, the photocurrent generated by PD also rises, causing the laser output to increase further until PD is saturated. This fast positive-feedback process very rapidly makes the output of LD jump from zero to a finite intensity. On the other hand, as the output of LD decreases, initially LD can maintain oscillation. When the laser output intensity weakens to less than the saturation point of PD, the photocurrent decreases significantly and the process reverses itself. The light output from LD jumps from a finite intensity back to zero due to this strong feedback. Therefore, we obtained a bistable hysteresis curve and observed the optical bistability output.

Figure 2 shows the bistable "laser output power  $P_0$  vs. bias  $V_A$ " of the IBILD as recorded by an x-y recorder. Figure 3(a) shows the bistable behavior of the "laser output power  $P_0$  vs. light signal input power  $P_i$ " of this device. From Figures 2 and 3(a) we know that the bistability width and output light

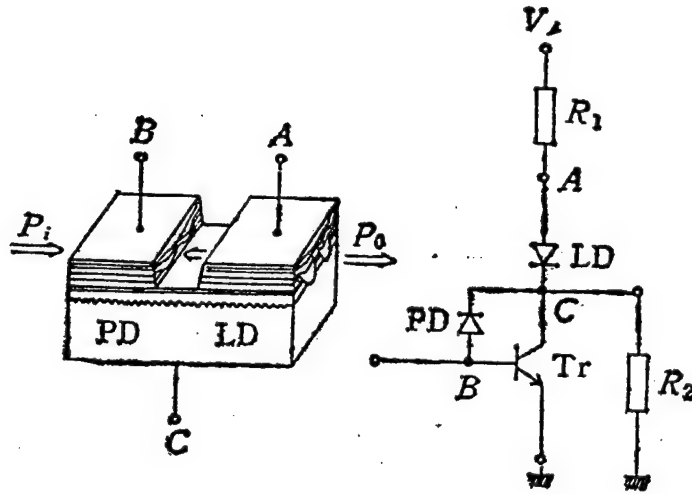


Figure 1. IBILD Structure and Its Associated Circuit

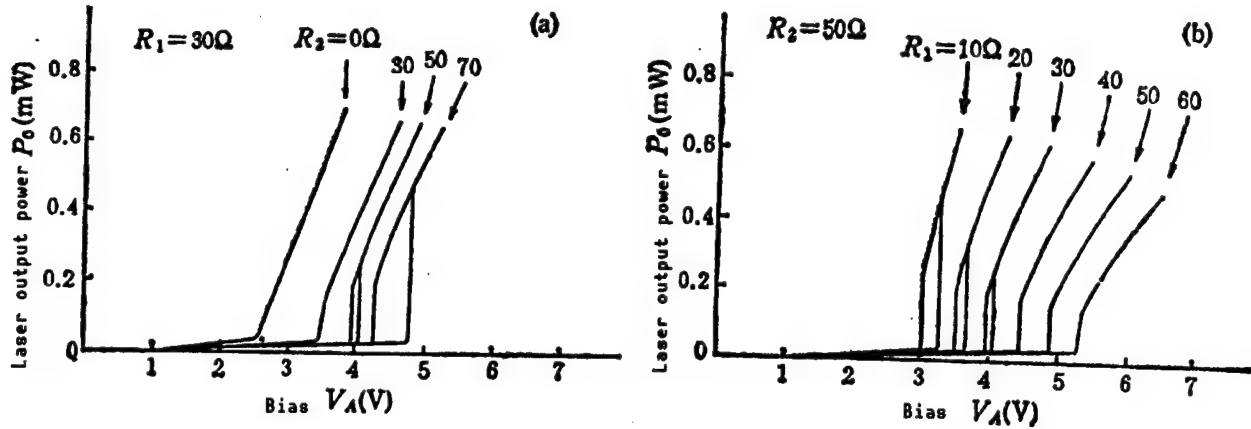


Figure 2. Bistability of Laser Output Power ( $P_o$ ) vs. Bias ( $V_A$ ) of IBILD Laser

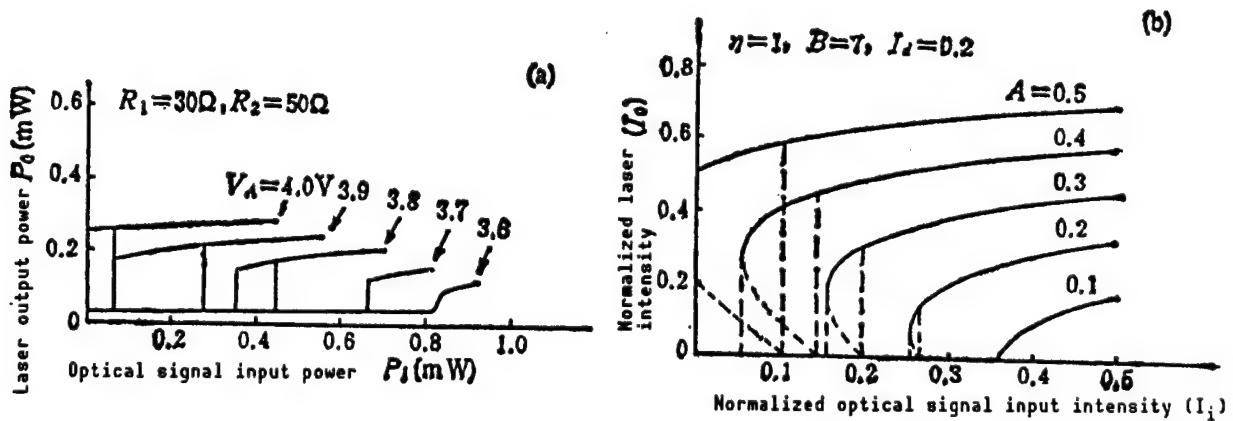


Figure 3. Bistability of Output Power vs. Optical Signal Input of IBILD Laser  
(a) Experimental; (b) Theoretical

intensity may be adjusted and controlled by varying the values of the resistance of  $R_1$  and  $R_2$  and the power supply voltage.

### III. Theoretical Rate Equations for Bistability

We have established a semiclassical theory for the distributed feedback-pumped bistable laser<sup>5</sup> and pointed out that this output feedback pumping method is applicable to any type of laser. Although the two-energy-level concept can still remain for a semiconductor laser, because these levels are distributed within a range described by a state density function, and because the probability of occupancy follows the Fermi-Dirac distribution instead of the simple bilevel Boltzmann distribution, the situation is much more complicated. Recently, we applied the rate equations for a semiconductor laser to the output feedback-pumped bistable semiconductor laser and obtained results that are consistent with experimental data. For a bistable semiconductor laser, the rate equations for the injected carrier concentration in the activated region and photo density  $S$  can be expressed as<sup>6</sup>:

$$\frac{dn}{dt} = \frac{J_p + J_f}{ed} - \frac{n}{\tau} - \xi a S (n - N) \quad (1)$$

$$\frac{dS}{dt} = \xi a S (n - N) - \frac{S}{\tau_p} \quad (2)$$

where  $J_p$  is the injection current density,  $d$  is the activation layer thickness,  $e$  is electron charge,  $\tau$  is carrier life,  $\xi$  is the laser mode-limiting factor in the activated region,  $a$  is a gain constant (to be determined by an optical transition cross section)  $\tau_p$  is the photon lifetime,  $N$  represents the carrier concentration to be injected in order to obtain the gain, and  $J_f$  is the injection current density produced by feedback pumping, which is related to the laser intensity. Furthermore, it satisfies the following equation:

$$J_f = \beta \frac{\eta I'_0 + I'_1}{1 + (\eta I'_0 + I'_1) / I'_d} \quad (3)$$

where  $\beta$  is the feedback pumping coefficient,  $\eta$  is the laser output feedback coefficient, and  $I'_0$ ,  $I'_1$ , and  $I'_d$  are the laser intensity, external input light signal intensity, and photodetector light saturation intensity, respectively.

Equations (1) and (2) neglect the effect of spontaneous radiation. From equations (1) and (2) it is possible to derive the steady-state photon density

$$S = \frac{\tau_p}{ed} (J_p + J_f - J_0) \quad (4)$$

where  $J_0$  is the threshold current density, and

$$J_0 = \frac{1 + \xi a N \tau_p}{\xi a \tau} \cdot \frac{ed}{\tau_p} \quad (5)$$

Hence, the laser intensity can be written as:

$$I'_0 = h\nu S v_g = h\nu v_g \frac{\tau_p}{ed} (J_p + J_f - J_0) \quad (6)$$

where  $v_g$  is the group velocity of light in the activation medium,  $h$  is Planck's constant, and  $\nu$  is the frequency of the laser mode. By normalizing the injection current density with respect to the threshold current density  $J_0$ , we get the following from (6) and (3):

$$I_0 = A + B \frac{\eta I_0 + I_i}{1 + (\eta I_0 + I_i) / I_d} - 1 \quad (7)$$

where  $A = J_p/J_0$  is the relative injection current density, or normalized pumping intensity,  $B = b\beta/J_0$  is the normalized feedback pumping coefficient, and  $I_0 = I'_0/b$ ,  $I_i = I'_i/b$ ,  $I_d = I'_d/b$  are the normalized laser intensity, normalized output light signal intensity, and normalized photodetector saturation light intensity, respectively. In the above equations,

$$b = h\nu v_g J_0 \frac{\tau_p}{ed} \quad (8)$$

The analytical solution of the normalized laser intensity  $I_0$  can be derived from (7).

$$I_0 = \frac{1}{2\eta} [(B\eta - 1) I_d - (1 - A)\eta - I_i] \pm \frac{1}{2\eta} \{ [(B\eta - 1) I_d - (1 - A)\eta - I_i]^2 - 4\eta [(1 - A)(I_d + I_i) - B I_d I_i] \}^{1/2} \quad (9)$$

This result is identical to the laser intensity equation of a feedback-pumped bistable laser that we previously derived from the quasi-classical theory.<sup>5</sup> The difference is that in the present equation, the parameters are determined by the corresponding parameters of the semiconductor laser.

In reference 5, we analyzed the stability of the laser intensity  $I_0$  as expressed by (9) and pointed out that when

$$B\eta > 1 \quad (10)$$

and

$$1 > A > 1 - \frac{I_i + (\sqrt{B\eta} - 1)^2 I_d}{\eta} \quad (11)$$

are met, it is possible to have bistable output. By properly selecting the values for  $A$ ,  $B$ ,  $\eta$ , and  $I_d$ , we can calculate the dependence of laser intensity  $I_0$  upon external input-signal light intensity  $I_i$ . The results are shown in Figure 3(b).

A comparison of the experimental result Figure 3(a) to the theoretical analysis 3(b) shows that bistability characteristics (including laser intensity and bistability width) vary with the pumping intensity of the laser according to very similar patterns.

#### IV. Conclusions

Stable and controllable optical bistability was achieved by using an integrated LD/PD and a simple circuit. The bistability width and output intensity can be adjusted over a wide range by varying the resistance of  $R_1$  and  $R_2$  or the power supply voltage  $V_A$ . As the study of surface-emission laser diode arrays progresses, the fabrication of an integrated optically bistable device consisting of a two-dimensional array of a large number of bistable elements is possible.

Acknowledgement: The authors wish to thank the Optoelectronics Research Institute of NEC Corporation for the assistance in fabricating the DFB-LD/PD.

#### References

1. A. Migus, A. Antonetti, D. Hulin, A. Mysyrowicz, H.M. Gibbs, N. Peyghambarian, and J.L. Jewell, APPL. PHYS. LETT., Vol 46, 1985, p 70.
2. W.F. Sharfin and M. Dagenais, Ibid., Vol 48, 1986, p 321.
3. H. Inaba, PHYS. LETT., Vol 86A, 1981, p 452.
4. H. Inaba, J. OPT. SOC. AM., Vol B1, 1984, p 467.
5. Yan Xuguang, H. Ito, and F. Inaba, JAPANESE JOURNAL OF COMMUNICATIONS TECHNOLOGY, OQE86-20, 1986.
6. Yasuharu Suematsu, "Semiconductor Laser and Integrated Optical Circuits," 191, Pub. by Omu-Sha, Tokyo, 1984.

## **Integrated Devices With Optical Dielectric Layers and MQW's**

90FE0172E Beijing BANDAOTI XUEBAO [CHINESE JOURNAL OF SEMICONDUCTORS] in Chinese Vol 11 No 4, Apr 90 (MS Received 9 May 89) pp 288-293

[Article by Lin Shiming [2651 0013 7686] of the Institute of Semiconductors of the Chinese Academy of Sciences: "Integrated Devices With Optical Dielectric Layers and Multiple Quantum Wells"]

### **[Text] Abstract**

An integrated reflective MQW device is designed by an optical transmission matrix method, and theoretical calculations are made. This device is fabricated by MOCVD [metal-organic chemical vapor deposition]. It consists of n-type anti-reflective coatings, i-type MQW's, and p-type high-reflectivity dielectric layers. The photocurrent and reflectivity spectra of the device have been obtained. They are compared to the theoretical results and found to be in good agreement. This device can be developed into a reflective integrated device capable of functions such as modulation, switching, and bistability.

**Key Words:** integration, MQW device, modulator.

### **I. Introduction**

Optical dielectric films have been widely used in the fabrication of optical elements for a long time. They are usually coated on the surface of an optical device by deposition in order to fabricate antireflective coatings, beam splitters, optical filters, and polarizers.

Recently, because of progress in semiconductor fabrication technology, abrupt-change thin films of precisely controlled thickness can be prepared by MBE [molecular beam epitaxy] and MOCVD. They are being more and more widely used in the fabrication of semiconductor optoelectronic devices.<sup>1</sup> Quantum well (layer thickness  $d < 100 \text{ \AA}$ ) and optical multiple dielectric layers (layer thickness  $d > 500 \text{ \AA}$ ) are planar multilayer in structure; they can be grown on the same substrate to fabricate various optoelectronic integrated devices by using compatible techniques.<sup>2,3</sup> The integrated reflective MQW optical modulator reported in this work is such an integrated optoelectronic device. It has a

potential to be widely used in two-way optical communication systems, optical switching arrays, and optical couplings. In this paper, the design and measured characteristics of the device are shown. Through testing of the multilayer dielectric film, the effect of uniformity of the MOCVD-grown layer is discussed. By measuring the photocurrent and reflectivity spectra of the modulator, the modulation ratio is estimated.

## II. Reflectivity of Multilayer Optical Dielectric Film

According to optical transmission theory, the transmission property of an optical thin film can be expressed as an optical matrix. When light at a wavelength  $\lambda$  shines upon a multilayer dielectric film (other layers are transparent), its transmission property is expressed in terms of a product of the optical matrix of each layer<sup>4</sup>:

$$\begin{bmatrix} \mu_1 \\ \mu_2 \end{bmatrix} = \prod_{\nu=1}^n \begin{bmatrix} \cos(\delta_\nu) & i \sin(\delta_\nu)/\Omega_\nu \\ i\Omega_\nu \sin(\delta_\nu) & \cos(\delta_\nu) \end{bmatrix} \cdot \begin{bmatrix} 1 \\ \Omega_{n+1} \end{bmatrix} \quad (1)$$

where the transmission phase factor of the  $\nu$ th layer is  $\delta_\nu = 2\pi\Omega_\nu d_\nu \cos(\theta_\nu)/\lambda$ , the optical capacitive reactance of the  $\nu$ th layer can be expressed as  $\Omega_\nu = n_\nu \cdot \cos(\theta_\nu)$  with respect to TE waves and  $\Omega_\nu = n_\nu/\cos(\theta_\nu)$  with respect to TM waves.  $\theta_\nu$  is the angle of refraction of the  $\nu$ th layer and  $n_\nu$  is the index of refraction of the  $\nu$ th layer. The equivalent optical capacitive reactance of the multilayer film  $\Omega$  can be determined from  $\Omega = \mu_2/\mu_1$ . Its reflectivity is

$$R = [(\Omega_0 - \Omega)/(\Omega_0 + \Omega)] \cdot [(\Omega_0 - \Omega)/(\Omega_0 + \Omega)]^* \quad (2)$$

A 1/4-wavelength-layer thickness multilayer film consisting of alternating high and low reflectivity material can result in a highly antireflective film. This is because of the coherent interference of the light reflected at an interface to the layer in front. Considering the fact that we are using GaAlAs to make MQW devices, similar materials are chosen to grow the highly antireflective film. The computer-calculated result based on equations (1) and (2) and the experimental data of the highly antireflective film grown by MOCVD are shown in Figure 1. Its structure is shown on the right as well. It consists of 10 cycles of AlAs (721 Å) and Ga<sub>0.9</sub>Al<sub>0.1</sub>As (614 Å). The indices of refraction used are their known published values.<sup>5</sup>

Although theoretical calculations show that the larger the two layers differ in index of refraction and the more layers there are, the higher the reflectivity of the multilayer film becomes, nevertheless, because GaAs is not transparent to the operating wavelength of the device (i.e., 860 nm), we chose Ga<sub>0.9</sub>Al<sub>0.1</sub>As, rather than GaAs, as the material for the high-reflectivity layer. From Figure 1 we can see that both calculated and test results show that high reflectivity is limited to a finite wavelength region, approximately 100 nm wide, near 860 nm. Nevertheless, the measured data is slightly less than the calculated result. Film reflectivity could reach as high as 95 percent. In this aspect, the measured data agrees well with the calculated result.



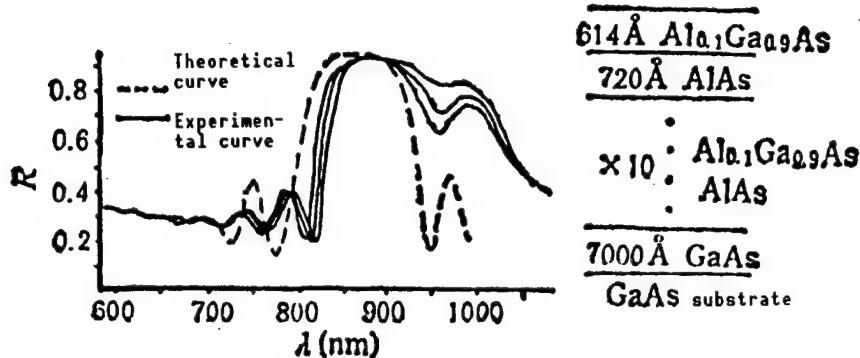


Figure 1. Calculated and Measured Reflectivity Spectra of the Highly Antireflective Film Upon Normal Incidence  
Its structure is shown on the right.

In addition, we can also see from Figure 1 that the measured reflectivity curve is leaning toward the longer wavelength side than the theoretical curve. Furthermore, different curves shown in the figure are measured results obtained from different locations on the film. The maximum deviation is approximately 10 nm. This point may be explained together with Figure 2. Figure 2 shows how the reflectivity of the multilayer film varies with the AlAs layer based on theory. It indicates that the high reflectivity shifts toward a longer wavelength as the layer thickness increases. The rate of change is approximately 6 nm (wavelength)/10 Å (thickness). The dependence on the  $\text{Ga}_{0.9}\text{Al}_{0.1}\text{As}$  layer thickness is similar. Therefore, the deviation between the measured data and the theoretical result, and the deviations of different measured curves, are due to the fact that the layer thickness grown is larger than the designed value and the layers are not uniform in thickness, respectively. According to calculation, the inhomogeneity of the layer thickness is less than 20 Å for that chip.

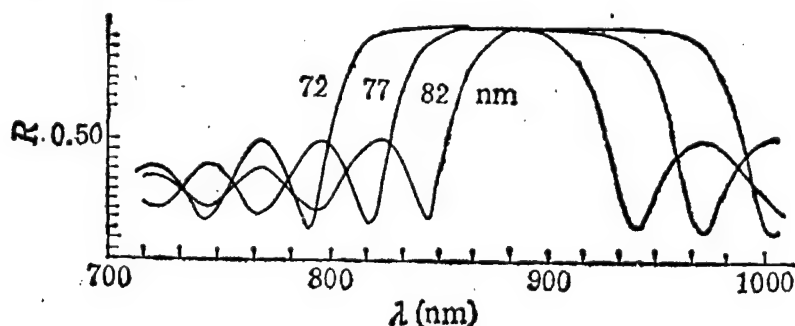


Figure 2. Calculated Reflectivity Spectrum of 1/4-Wavelength High-Reflectivity Film as a Function of AlAs Thickness

In the simple device design, when  $(n_h/n_l)^{2m} \cdot (n_s/n_0) \gg 1$ , the bandwidth of high reflectivity and maximum reflectivity can be estimated by the following two equations:

$$\text{bandwidth } \Delta = (4\lambda/\pi) \sin^{-1}[(n_h - n_l)/(n_h + n_l)] \quad (3)$$

$$\text{maximum } R = 1 - 4(n_l/n_h)^{2m} \cdot (n_0/n_s) \quad (4)$$

where  $n_h$  and  $n_l$  are the indices of refraction of the high and low refractive layers, respectively;  $m$  is the number of cycles; and  $n_0$  and  $n_s$  are the dielectric constants of the incident medium and the substrate, respectively. For example, based on these two equations we can estimate that the bandwidth of the multilayer film shown in Figure 1 is 91 nm and the maximum reflectivity is 95 percent. Hence, these two equations are quite accurate.

### III. Structural Design of an Integrated Reflective MQW Modulator

The design of the integrated reflective MQW modulator is a PIN diode consisting of n-type antireflective layers, i-type MQW's, and p-type high-reflectivity layer. The device was fabricated by MOCVD on an n-type substrate doped with  $10^{18}$  Si. This is a reversed structure modulator. The antireflective film was grown to facilitate the coupling of light over the specified band for the device. In order to simplify the fabrication process, the antireflective film ( $4 \times \text{Ga}_{0.9}\text{Al}_{0.1}\text{As}/\text{Ga}_{0.5}\text{Al}_{0.5}\text{As}$ ) was designed in a manner similar to the high-reflectivity film. It is made of alternating low and high index of refraction materials and the thickness of such twin layers is  $1/4$  wavelength. However, the low index of refraction layer must be the first layer. The transmission characteristics of the antireflective film are shown in Figure 3. The minimum reflectivity was designed at 860 nm. Because the exciton absorption peak is there, the modulator also operates in that vicinity.

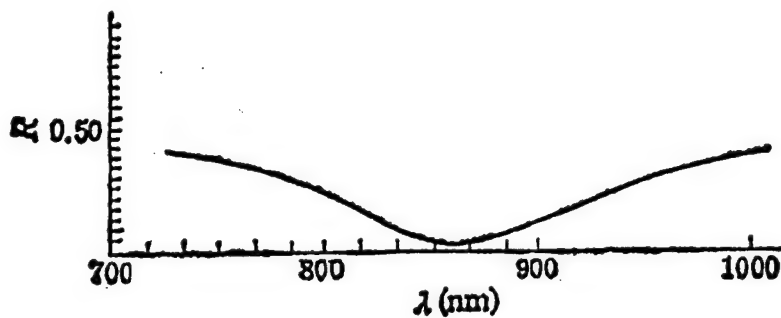


Figure 3. Calculated Reflectivity Spectrum of the Transmission Film Consisting of Four  $1/4$ -Wavelength Layers

The design of the i-type quantum wells primarily involves the selection of the width, depth, number of the wells, and the barrier width. The principle of calculation is as follows.<sup>1</sup> The foundation of a quantum-well modulator is the quantum confined Stark effect, i.e., the variation of the energy of quantized energy levels in the well (including two-dimensional exciton) under an external electric field and the associated transition probability. Hence, it is necessary to solve the following equation:

$$H\psi - E\psi$$

where  $H$  is the effective electron-hole mass Hamilton when an electric field  $F$  is applied on the quantum-well material along the  $z$ -direction perpendicular to the well. It may be expressed as:

$$\begin{aligned}
 H &= H_e + H_h + H_{eh} \\
 &= -\frac{\hbar^2}{2m_{e\perp}^*} \frac{\partial^2}{\partial z_e^2} + V_e(z_e) + eFz_e \\
 &\quad -\frac{\hbar^2}{2m_{h\perp}^*} \frac{\partial^2}{\partial z_h^2} + V_h(z_h) - eFz_h \\
 &\quad -\frac{\hbar^2}{2\mu} \frac{\partial^2}{\partial r^2} - \frac{e^2}{e(|z_e - z_h|^2 + r^2)^{1/2}}
 \end{aligned} \tag{5}$$

where  $\mu = \frac{m_{e\parallel}^* m_{h\parallel}^*}{m_{e\parallel}^* + m_{h\parallel}^*}$

In the above equation,  $H_e$  and  $H_h$  are the potential and kinetic energy Hamilton for the electron and hole, respectively.  $H_{eh}$  is the Hamilton for the relative motion and Coulombic effect between electron and hole.  $z_e$  and  $z_h$  are the  $z$  component of the positions of electron and hole, respectively.  $V_e(z_e)$  and  $V_h(z_h)$  are the potential barriers confining electron and hole, respectively.  $r$  is the relative position of electron and hole on the  $x, y$  plane.  $m_{e\perp}^*$ ,  $m_{h\perp}^*$ , and  $m_{e\parallel}^*$ ,  $m_{h\parallel}^*$  are the effective mass of electron and hole in the  $z$ -direction and on the  $x, y$  plane, respectively.

Let us assume

$$\Psi(z_e, z_h, r, F) = \psi_e(z_e, F) \cdot \psi_h(z_h, F) \cdot \phi_{eh}(r, F) \tag{6}$$

First, let us solve  $\psi_e(z_e, F)$  and  $\psi_h(z_h, F)$ . They can be determined from the following equations:

$$\begin{cases} H_e \psi_e(z_e, F) = E_e \psi_e(z_e, F) \\ H_h \psi_h(z_h, F) = E_h \psi_h(z_h, F) \end{cases}$$

In order to minimize the computation load, the system can be approximated by an infinitely deep potential well. At the same time, in order to minimize the error, an effective well width method is used. The solutions to the above equations are

$$\begin{cases} \psi_e(z_e, F) = a_e(F) A_i(z_e) + b_e(F) B_i(z_e) \\ \psi_h(z_h, F) = a_h(F) A_i(z_h) + b_h(F) B_i(z_h) \end{cases} \tag{7}$$

where  $A_i(z)$  and  $B_i(z)$  are the first and second type Airy functions. The coefficients  $a_e$ ,  $b_e$ ,  $a_h$ , and  $b_h$  are determined by the boundary and normalization conditions. Hence, the wave functions  $\psi_e$  and  $\psi_h$  can be obtained.

Then, let us find  $\phi_{eh}(r, F)$ . It is in the form of the  $1s$  wave function of a planar hydrogen-like atom by using the exciton radius  $\lambda(F)$  instead of the Bohr radius:

$$\phi_{eh}(r, F) = \sqrt{\frac{2}{\pi}} \cdot \frac{1}{x} e^{-r/\lambda} \quad (8)$$

Substituting equations (7) and (8) into (6) and then into  $\left\langle \psi \left| \frac{-e^2}{\epsilon(|z_o - z_h|^2 + \gamma^2)^{1/2}} \right| \psi \right\rangle$  and differentiating with respect to  $\gamma$ , the exciton binding energy can be obtained. The exciton energy under a given electric field can be then determined. When the conduction band to valence band discontinuous energy ratio is 57:43 and  $m_e^* = 0.0665m_0$ ,  $m_{hh1}^* = 0.34m_0$ ,  $m_{hh1}^* = 0.1m_0$ ,  $m_{hv1}^* = 0.094m_0$ ,  $m_{hv1}^* = 0.2m_0$ ,  $L = 105 \text{ \AA}$ ,  $V_e = 228 \text{ meV}$ ,  $V_h = 172 \text{ meV}$ , the rate of change of exciton energy level as a function of applied external voltage can be calculated to be  $d\gamma/dV \approx 1.25 \text{ nm/V}$ .

The above calculation is based on a MQW region and  $60 \times 105 \text{ \AA}$  GaAs/60  $\text{\AA}$   $\text{Al}_{0.3}\text{Ga}_{0.7}\text{As}$  structure. The potential barrier width was chosen to avoid coupling between wells and the number of wells was chosen to have an effective working area.

The p-type highly antireflective film is composed to multiple layers of the AlAs/Ga<sub>0.9</sub>Al<sub>0.1</sub>As bilayer structure described before. However, because the incident medium is the MQW material, instead of air, the 10-cycle structure described above no longer has a reflectivity of 95 percent. Instead, it drops down to 85 percent, therefore, the number of layers is increased to 12. Furthermore, a P-type GaAs layer was grown on the P-type antireflective film to facilitate the fabrication of a P-type electrode. The other electrode was directly connected to the n-type substrate. A reverse bias was applied to the device and the breakdown voltage of the device was measured to be more than 30 V.

#### IV. Characteristics of Integrated Reflective MQW Modulator

The transmission characteristics of the device have been calculated based on equations (1) and (2). Originally, the MQW region is a multilayer film with 60 cycles of bilayer structure. However, our calculations show that the computation would not be affected if it is treated as a uniform medium with an effective index of refraction of  $n_{eff} = (n_w \cdot d_w + n_b \cdot d_b) / (d_w + d_b)$ , where  $n_w$ ,  $d_w$ , and  $n_b$ ,  $d_b$  are indices of refraction and widths of the well region and barrier region, respectively. Hence, the amount of computation was drastically reduced.

Figure 4 shows the structure of the device, and the theoretical and experimental transmission characteristics of the device. Because the MQW material was treated as a transparent medium in the calculation, there is good agreement between calculated and experimental results when the wavelength is longer than 860 nm. As for wavelength less than 860 nm, absorption between exciton and the energy band plays a dominant role. In particular, the rapid drop of reflectivity at 860 nm is attributed to exciton absorption. Valleys  $\alpha$  and  $\beta$  correspond to the transition of electron from conduction band to heavy-hole band and light-hole band, respectively.

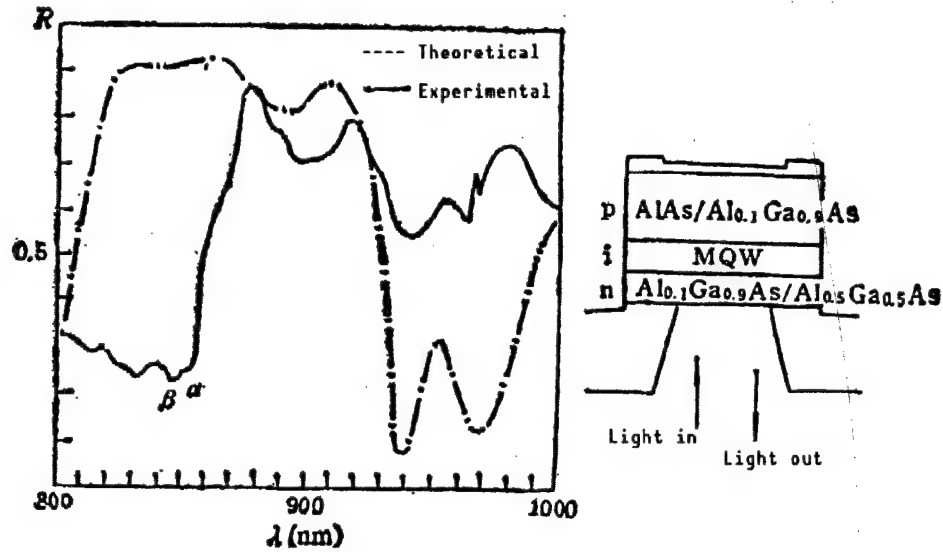


Figure 4. Calculated and Measured Reflectivity Spectra of the Integrated Reflective MQW Device.  
The device structure is shown on the right.

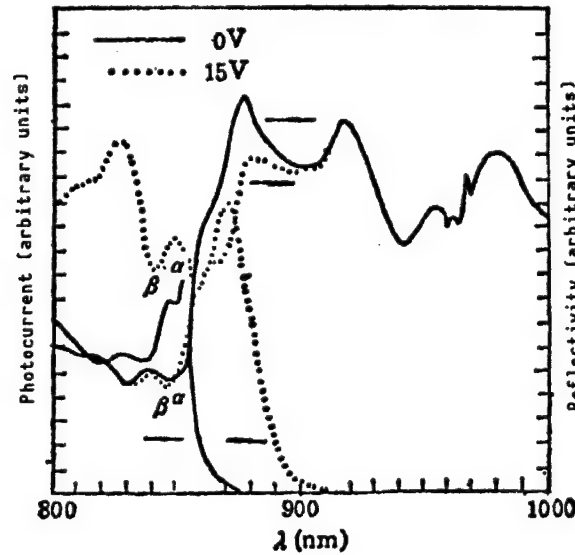


Figure 5. Photocurrent and Reflectivity Spectra of the Integrated MQW Device at Different Reverse-Bias Voltages

Figure 5 shows the measured photocurrent and reflectivity spectra of the device under different bias voltage. This figure not only shows the modulation effect of the device but also explains the cause of modulation. From the photocurrent spectra, when a reverse bias (-15 V in the figure) is applied to the device, due to the quantum Stark effect in the external electric field, the exciton absorption peak shifts toward longer wavelength, which causes a drop of reflectivity at the corresponding wavelength (such as  $\lambda = 870$  nm in

the figure). Thus, absorption modulation of reflected light to incident light is realized.<sup>6,7</sup> In addition, the figure also shows that such a modulator may have two different modulation effects at different operating wavelength bands. At 850-857 nm, an increase in bias voltage causes the reflectivity to rise. This is a positive modulation effect. At 857-890 nm, an increase in bias voltage causes the reflectivity to decline. This is a negative modulation effect. The presence of such different modulation effects may allow us to develop this device into a switch or a bistable device. The switching and bistability characteristics of this device will be discussed separately. Based on experimental data, the change in reflectivity (rate of modulation) of the device in these two wavelength bands could reach 2.2 dB when the bias is increased from 0 V to 15 V.

## V. Conclusions

Because the optical multilayer dielectric film and the quantum wells are of a flat multilayer structure and can be compatibly grown on the same substrate to fabricate various integrated optoelectronic devices to allow some transmission devices to become reflective devices, they denote an important structure in optoelectronic integration. This type of device can be designed by using an optical transmission matrix. This paper reports the fabrication of such a device with MOCVD and shows the photocurrent and reflectivity spectra measured. The results are in good agreement with theoretical calculations. Reflectivity spectra of the device show both positive and negative modulation. Therefore, the device can have a combination of functions, including modulation, switching, and bistability.

## References

1. D.A.B. Miller, D.S. Chemla, T.C. Damen, T.H. Wood, C.A. Burrus, A.C. Gossard, and W. Wiegmann, *IEEE J.*, Vol QE-21, 1985, p 1462.
2. R.L. Thornton, R.D. Burnham, and W. Streifer, *APPL. PHYS. LETT.*, Vol 45, 1984, p 1028.
3. G.D. Boyd, D.A.B. Miller, D.S. Chemla, S.L. McCall, A.C. Gossard, and J.H. English, *Ibid.*, Vol 50, 1987, p 1119.
4. M. Born and E. Wolf, "Principles of Optics," 1980, 6th Ed.
5. A.N. Pikhtin and A.D. Yaskov, *SOV. PHYS. SEMICOND.*, Vol 14, 1980, p 389.
6. D.A.B. Miller, D.S. Chemla, T.C. Damen, A.C. Gossard, W. Wiegmann, T.H. Wood, and C.A. Burrus, *PHYS. REV.*, Vol B32, 1985, p 1043.
7. P.J. Braddley, P. Wheatley, G. Parry, J.E. Midwinter, P. Mistry, J.S. Roberts, *ELECTRONICS LETTERS*, Vol 23, 1987, p 213.

## Visible Terraced Substrate Inner Stripe Semiconductor Laser

90FE0172F Beijing BANDAOTI XUEBAO [CHINESE JOURNAL OF SEMICONDUCTORS] in Chinese Vol 11 No 4, Apr 90 (MS Received 17 Mar 89) pp 311-315

[Article by Du Guotong [2629 0948 0681], Zhang Xiaobo [1728 2556 3134], Zhao Fanghai [6392 2455 3189], Zou Zheng [6760 1513], and Gao Dingsan [7559 7307 0005] of the Department of Electronic Science, Jilin University: "Visible Terraced Substrate Inner Stripe Semiconductor Laser"]

### [Text] Abstract

The novel semiconductor laser design, the terraced-substrate inner stripe (TSIS) laser, has been expanded into the visible region (0.75~0.80  $\mu\text{m}$ ). The lowest dc threshold current is 26 mA, the linear laser power output range is 15~20 mW, and the fundamental mode can operate at 2~4  $I_{\text{th}}$ . At 4 mW, the operating lifetime has exceeded 5,000 hours. The paper also analyzes ways to improve the reliability of the device.

Key Words: visible light, terraced substrate, inner stripe, semiconductor laser.

### [Text] I. Introduction

The visible laser is the most widely used semiconductor laser in information processing. Nevertheless, China does not have any production capability. Therefore, the development of a simple and reliable visible laser with good behavior is an issue to be dealt with at the present time. We have successfully extended the novel TSIS laser structure into the visible region.

### II. Fabrication Technique

A P-type Zn-doped GaAs single-crystal wafer with a carrier concentration of  $1\sim2 \times 10^{19} \text{cm}^{-3}$  was used as the substrate. A solution made of 1:8:8 ( $\text{H}_2\text{SO}_4:\text{H}_2\text{O}_2:\text{H}_2\text{O}$ ) was used to etch a 2.5~3- $\mu\text{m}$  deep inverted trapezoidal trench (dovetail trench). Two chips share one common trench, which is 250~350  $\mu\text{m}$  wide. Prior to epitaxy, the surfaces were etched for approximately 1 minute in an alkaline solution comprised of  $\text{NaOH}:\text{H}_2\text{O}_2:\text{H}_2\text{O} = 0.5\text{g}:0.5\text{ml}:10\text{ml}$ . An extrusion plate was used in epitaxy. Growth began at 815°C and five epitaxial layers were grown at

a cooling rate of  $0.3^{\circ}\text{C}/\text{minute}$ . The first layer is an n-type GaAs current barrier which is doped with Te at a carrier concentration of  $4 \times 10^{18}\text{cm}^{-3}$ . It is  $0.6\text{--}1\ \mu\text{m}$  thick in the flat area. During the growth of the first layer, it is necessary to keep  $3\text{--}6^{\circ}\text{C}$  of super-cooling. The growth time must be kept short in order not to grow anything on the shoulder of the trench to form a natural current path. The second layer is a P-type  $\text{Al}_y\text{Ga}_{1-y}\text{As}$  lower confinement layer which has a carrier concentration of  $2 \times 10^{18}\text{cm}^{-3}$ . The mesa thickness is controlled to be within  $0.15\text{--}0.4\ \mu\text{m}$ . The selection of a P-type dopant in this layer is also a research topic. Previously, when we fabricated the  $0.88\text{-}\mu\text{m}$  device,<sup>1</sup> we used Ge. Now in the  $0.78\text{-}\mu\text{m}$  [wavelength] device we are fabricating, the active region is doped with Al, and the Al content in the confinement layer must also increase correspondingly to a value  $y$  of approximately 0.5. An increase in the activation energy of Ge can hardly produce such a high carrier concentration. The activation energy of Zn is lower; however, its vapor pressure is too high, which can easily result in contamination. Therefore, we switched to Mg as the dopant. The doping characteristics of Mg in  $\text{Al}_y\text{Ga}_{1-y}\text{As}$  layers prepared by liquid phase epitaxy (LPE) at  $700^{\circ}\text{C}$  and  $780^{\circ}\text{C}$  have been analyzed by Chinese scholars<sup>2,3</sup>; however, the data is not very consistent. We studied the Mg doping characteristics at  $815^{\circ}\text{C}$ , the temperature at which the layer is actually grown. Figure 1 shows the dependence of carrier concentration upon the aluminum content  $y$  at a fixed Mg gram molar ratio of  $1.3 \times 10^{-3}$ . Figure 2 shows the dependence of carrier concentration upon the Mg dopant content at a fixed Al content of  $y \pm 0.5$ . The third layer is the  $\text{Al}_x\text{Ga}_{1-x}\text{As}$  active region. The wavelength of the laser is dependent upon the Al content  $x$  in the active layer. We have conducted experiments on this subject and have reported the results in reference.<sup>4</sup> The  $0.2\text{-}\mu\text{m}$  thick active region is doped with Mg and has a carrier concentration of  $1 \times 10^{18}\text{cm}^{-3}$ . The fourth layer is an n-type  $\text{Al}_y\text{Ga}_{1-y}\text{As}$  upper-confinement layer, which is doped with Te at a carrier concentration of  $2 \times 10^{18}\text{cm}^{-3}$  and which has a thickness of approximately  $1\ \mu\text{m}$ . The fifth layer is an n-type GaAs cover layer, which is doped with Te at a carrier concentration of  $4 \times 10^{18}\text{cm}^{-3}$  and is  $3\text{--}5\ \mu\text{m}$  thick. After the growth of the epitaxial layer, the ohmic contacts are made directly by depositing Au-Ge-Ni on the n side and Au-Zn-Au on the P side. The wafer is then sliced for assembly.

### III. Device Characteristics

#### 1. V-I Characteristics

The wavelength of the device developed is  $0.75\text{--}0.80\ \mu\text{m}$ . The forward turn-on voltage is  $1.4\text{--}1.7\ \text{V}$  and the reverse breakdown voltage is approximately  $10\ \text{V}$ . The breakdown voltage of the current breakdown layer is  $12\text{--}16\ \text{V}$ , which can effectively confine the current.

#### 2. Threshold Characteristics

The internal current path in this device is very narrow, only  $1\text{--}2\ \mu\text{m}$ ; therefore, the threshold current is very low. A batch of room-temperature continuous-wave (CW) devices has been fabricated with thresholds ranging from  $30\text{--}50\ \text{mA}$ . The lowest threshold is  $26\ \text{mA}$ . We have obtained laser diodes whose pulsed thresholds are as low as  $11\ \text{mA}$  and  $16\ \text{mA}$ .



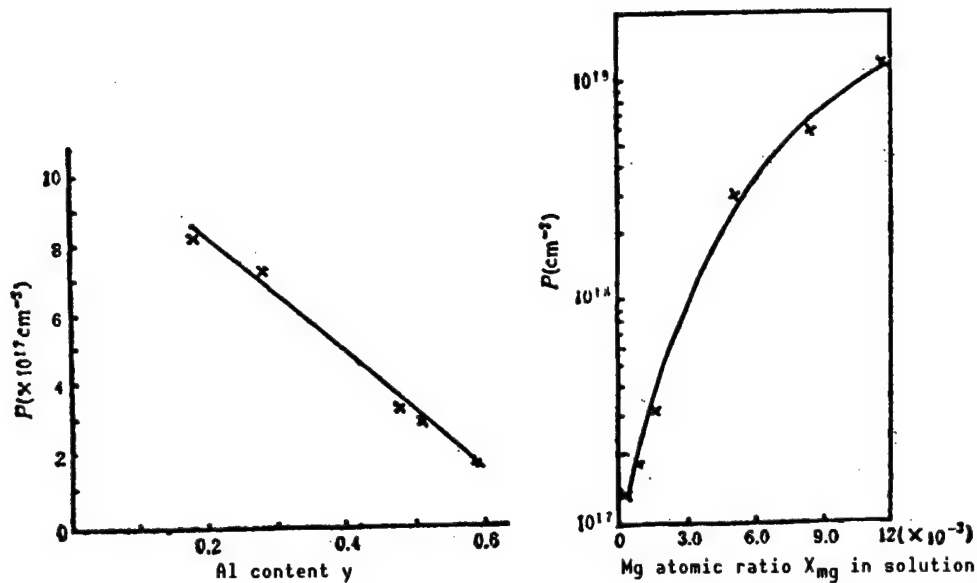


Figure 1. Carrier Concentration vs. Al Content

Figure 2. Mg Content in Mother Liquid vs. Carrier Concentration

### 3. Optical-Electrical Characteristics

The curve for the visible TSIS laser's linear light output power vs. current shows good performance. The linear power range goes up to 15-20 mW. The maximum output power could reach over 30 mW. The external differential quantum efficiency is 30-50 percent (both sides). Figure 3 shows the light power curves of several devices.

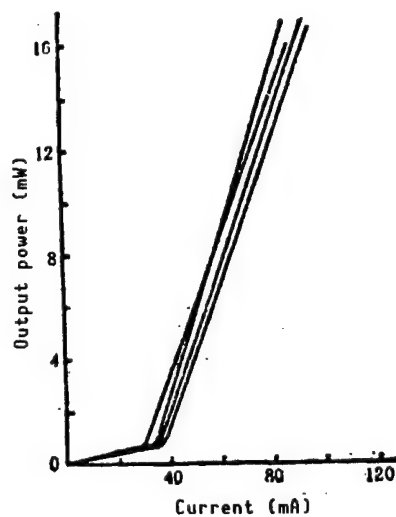


Figure 3. Power vs. Current Curves for Visible TSIS Lasers

#### 4. Mode Characteristics

**Transverse Mode:** The visible TSIS laser can oscillate quite well in its fundamental mode over a large current range ( $2\sim 4 I_{th}$ ). The horizontal divergence angle is  $10\sim 15^\circ$  and the vertical divergence angle is  $25\sim 40^\circ$ . Figure 4 shows the far-field angular light intensity distributions of the visible TSIS laser.

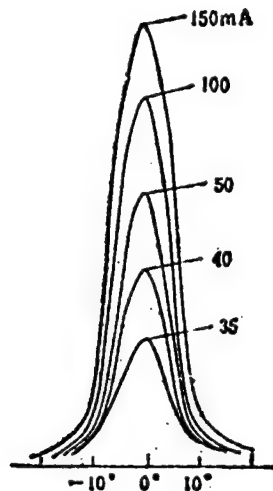


Figure 4. Far-Field Angular Light Intensity Distribution of the Visible TSIS Laser

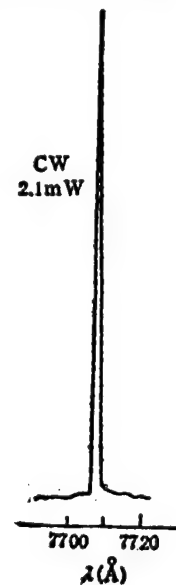


Figure 5. Spectrum of Visible TSIS Laser

**Longitudinal Mode:** Because a good ridge waveguide can be incorporated in the device, excellent single longitudinal model (SLM) laser emission can be obtained at low power. Figure 5 shows the spectrum of a laser in CW operation at room temperature. Some fundamental-mode lasers operated in symmetric multiple longitudinal modes.

#### IV. Reliability of Device

Reliability is an important factor determining whether a device is practical. Because the active region of the (GaAl)As visible laser is doped with Al, the Al content in the confinement layer must also be raised. Hence, lattice mismatch is getting larger. Consequently, stress and defects also go up. Therefore, lifetime is a problem of concern and cannot be easily resolved. The visible TSIS laser was specifically designed and developed to improve this problem.

In many laser structures fabricated by one-step LPE, such as CSP, TS, CS, and CDH, because electrode stripes must be prepared using techniques such as deposition masking, photolithography, and Zn diffusion after the epitaxial wafer is grown, more stress and defects are introduced to the crystal during these high-temperature processes to adversely affect the reliability of the device. Furthermore, these devices use n-type GaAs as the substrate. The

lower-confinement layer  $\text{Al}_y\text{Ga}_{1-y}\text{As}$  layer is also n-type. It is necessary to dope Te in the Al layer to achieve the desired carrier concentration. However, Te has a high distribution index which becomes an impurity that can be easily segregated. A high-concentration doping of Te often results in the deterioration of the epitaxial layer and the surface becomes uneven. If an active layer is grown on top of such an epitaxial layer, the quality of the active layer will be adversely affected and interfacial scattering loss will also increase.<sup>5</sup> In order to investigate the quality of the Te-doped  $\text{Al}_x\text{Ga}_{1-x}\text{As}$  epitaxial layer, a comparison of Zn diffusion in Te-doped and Sn-doped  $\text{Al}_x\text{Ga}_{1-x}\text{As}$  epitaxial layer was made and the results are shown in Figure 6 [photo not reproduced]. Figure 6(a) is a picture of the Zn diffusion junction in an Sn-doped  $\text{Al}_x\text{Ga}_{1-x}\text{As}$  layer. We can see that the surface of the epitaxial layer is smooth and the leading edge of diffusion is also uniform, indicating the crystal quality of the epitaxial layer is quite good. Figure 6(b) is a picture of the Zn diffusion junction on the  $\text{Al}_x\text{Ga}_{1-x}\text{As}$  epitaxial layer. The surface is uneven and the diffusion leading edge is not uniform. This indicates that the crystal quality is not uniform and there are more defects. These defects would capture Zn atoms to lower the diffusion rate and make the Zn junction line uneven.<sup>6</sup> Therefore, it is very difficult to fabricate high-reliability visible light lasers on an n-type GaAs substrate.

The VSIS (V-channel substrate inner stripe) laser diode employs a two-step epitaxial process to fabricate the internal current path to partially overcome the above problem. However, two-step epitaxy is a very problematic technology and usually takes a long time. Furthermore, it is not very easy to thoroughly clean the part after the first step, affecting the quality of the second step. This also has an adverse impact on its reliability.

The TSIS laser developed has overcome the deleterious effect of the VSIS method introduced by two-step epitaxy. Afterward, there is no need for additional processes such as mask deposition and Zn diffusion. Thus, adverse effects introduced by these processes on lattice defects and stress can be avoided. The TSIS structure uses a P-type substrate. The n-type Te-doped  $\text{Al}_y\text{Ga}_{1-y}\text{As}$  upper-confinement layer is grown on top of the active layer. Problems such as Te segregation would not affect the quality of the active layer. Furthermore, the light emitting area is located at the shoulder angle of the substrate channel. At the shoulder, it is slightly re-melted before epitaxial growth. This slight re-melting is the best substrate surface treatment which will enhance the quality of the crystal grown. Therefore, the TSIS structure can improve the reliability and increase the lifetime of the device.

The reliability of TSIS lasers of various wavelengths is being evaluated (research still in progress). The work shows that devices operating in the 0.78  $\mu\text{m}$  to 0.80  $\mu\text{m}$  wavelength range have higher reliability. Figure 7 shows the performance of two 0.78- $\mu\text{m}$  wavelength devices operating at 55°C at 3 mW as a function of time. After operating at 55°C for 150 hours (extrapolated to more than 4,000 hours at room temperature), these devices were operated for nearly 1,000 hours at room temperature (23-29°C) at 3 mW and the threshold still only varies slightly. Figure 8 shows the current-versus-time curve for a 0.80- $\mu\text{m}$  wavelength device. The threshold current for this device is 50 mA and it was operated for 1,248 hours at 1.3 mW; the operating current still

remained at 55–56 mA. Afterward, it was switched to operate at 4 mW for over 5,000 hours; the operating current remained at approximately 72 mA with little change. The lifetime of such a device should reach tens of thousands of hours. This is a breakthrough in our laboratory in the development of GaAs lasers (including 0.85–0.88  $\mu\text{m}$ ) wave band of various structures (including VSIS structure) using our simple facilities. This fully demonstrates that this structure can effectively improve the reliability and increase the useful lifetime of visible lasers. Of course, the lifetime is dependent upon the wavelength of the laser. High-temperature aging screening shows that reliability remains to be an issue for lasers operating at 0.75  $\mu\text{m}$ . At 0.76  $\mu\text{m}$  and 0.77  $\mu\text{m}$ , the fraction of better-reliability lasers is significantly less. There are still problems to be further investigated.

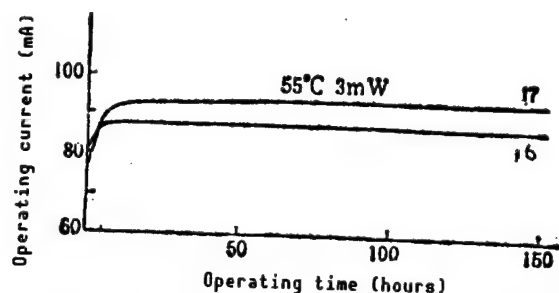


Figure 7. High-Temperature Aging Current vs. Time for 0.78- $\mu\text{m}$  Laser

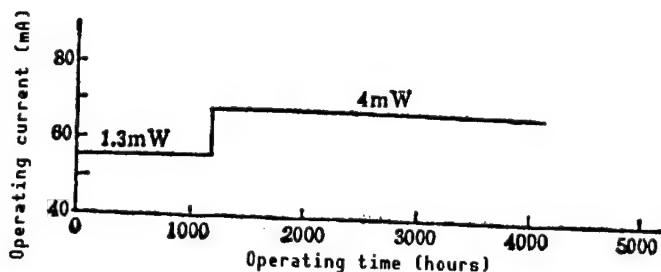


Figure 8. Room-Temperature Operating Current vs. Time of 0.80- $\mu\text{m}$  Wavelength Laser

## V. Conclusion

The TSIS laser has been extended to the visible region. The wavelength range of the device is 0.75–0.80  $\mu\text{m}$ . The lowest threshold current is 26 mA at room temperature. Pulsed threshold currents as low as 11 mA and 16 mA have been achieved. The linear light power output goes up to 15–20 mW. Fundamental mode oscillation can be maintained at four times threshold current. At low power, the device can emit laser light in SLM. A lifetime evaluation shows that the device has a higher reliability in the 0.78–0.80  $\mu\text{m}$  band. At room temperature, the operating lifetime can exceed 5,000 hours, or even up to 10,000 hours, at 3–4 mW. The results further prove that the TSIS structure is an excellent advanced laser, especially in terms of improved reliability. Furthermore, it is simple, fast and easy to fabricate. It also conserves raw materials and power.

The authors wish to thank Yang Jian [2799 1696], She Hui [0152 6540], and Wang Wen [3769 2429] for performing some experimental work.

#### References

1. Du Guotong, Ma Xiaoyu [7456 7522 1342], Zou Zheng, and Gao Dingsan, BANDAOTI XUEBAO [CHINESE JOURNAL OF SEMICONDUCTORS], Vol 9 No 3, 1988, p 335.
2. Liu Hongxun [0491 1347 8113], Zhang Bei [4545 5563], Wang Shumin [3769 5289 3046], and Yu Lisheng [5713 6786 3932], Ibid., Vol 8 No 2, 1987, p 214.
3. Yu Jinzhong [0151 6855 0022], Sohachi Iwai, and Y. Aoyagi, Ibid., Vol 6 No 2, 1985, p 123.
4. Ma Xiaoyu, Du Guotong, and Gao Dingsan, BANDAOTI GUANGDIAN [SEMICONDUCTOR OPTOELECTRONICS], Vol 9 No 2, 1988, p 4.
5. T. Hayakawa, N. Miyauchi, S. Yamamoto, H. Hayashi, S. Yano, and T. Hijikata, J. APPL. PHYS., Vol 53 No 11, 1982, p 7224.
6. S.P. Lee, et al., SOLID STATE ELECTRONICS, Vol 21 No 6, 1978, p 905.

# **Monolithic Integration of Amplifier With MSM-PD on GaAs**

90FE0172G Beijing BANDAOTI XUEBAO [CHINESE JOURNAL OF SEMICONDUCTORS] in Chinese Vol 11 No 5, May 90 (MS Received 6 Apr 89) pp 395-398

[Article by Yang Qinqing [2799 3084 3237] and Gao Junhua [7559 0193 5478] of the Institute of Semiconductors of the Chinese Academy of Sciences, funded by the Chinese Natural Science Foundation: "Monolithic Integration of Amplifier With MSM-PD on GaAs"]

## **[Text] Abstract**

This paper describes a simple GaAs MSM-PD (metal-semiconductor-metal photodiode) which is compatible with the GaAs MESFET [metal semiconductor field-effect transistor] fabrication technique. It can detect short-wavelength laser light. The characteristics of the MSM-PD are discussed. In addition, the monolithic integration of the MESFET amplifier circuit is also described. Finally, preliminary results obtained with integrated diodes are also reported.

**Key Words:** monolithic integration, metal-semiconductor-metal photodiode (MSM-PD), MESFET (metal semiconductor field-effect transistor), tungsten silicide.

In recent years, the optoelectronic integrated circuit (OEIC) has attracted general attention. It has a bright prospect in high-speed, large-capacity optical communications, and data processing. The main advantage of integration is to reduce limiting speed, noise generation, and parasitic impedance. Also, it can further reduce the size and improve the reliability of such a device. Monolithic integration of laser-driving circuit and detector (such as PIN or APD)-amplifier has been developed. In OEIC devices, optical devices such as lasers and PIN detectors are longitudinal structure devices. Nevertheless, driving circuits and amplifiers comprised of MESFET's are transverse devices. These two types of devices are structurally and technologically incompatible. This makes the monolithic integration of optoelectronic devices more difficult. This paper reports a monolithically integrated MSM-PD with an amplifier comprised of a GaAs MESFET. The MSM-PD is used as a detector. It is compatible with a MESFET both in structure and in fabrication technology, which makes monolithic integration easy.

## I. Structure and Performance of the MSM-PD

The MSM-PD is structurally very simple. A MSM-PD can be fabricated by forming two sets of staggered comb-shaped electrodes on a semi-insulating GaAs substrate or on the GaAs buffer layer of an epitaxial structure. These two sets of electrodes and the high-resistance GaAs surface create a Schottky contact, thus forming two back-to-back Schottky diodes as shown in Figure 1. When light of a fixed wavelength shines on the GaAs between these electrodes, photon-induced carriers will be produced. These carriers drift toward the electrodes under the applied electric field to form a photocurrent. This photocurrent,  $I_p$ , is a function of applied external bias  $V_1$  and input light power  $W_L$ . If ion implantation is used to prepare the GaAs circuit, it is very easy to fabricate the MSM-PD on the semi-insulating GaAs. In this work, WSi<sub>x</sub> [tungsten silicide] electrodes, 4  $\mu\text{m}$  wide and 4  $\mu\text{m}$  apart, were directly prepared on a semi-insulating GaAs surface covering a light-sensitive area of 140  $\mu\text{m}$  x 140  $\mu\text{m}$ . This type of MSM-PD usually has a breakdown voltage of greater than 50 volts. The dark current is usually between 10 and 20 nA when  $V_1 = 5\sim 20$  V. Figure 2 shows the photocurrent  $I_p$  vs. input light power  $W_L$ , which is linear. From the figure, the sensitivity of the device is 0.22 A/W. Because some light is blocked by the electrodes, the actual sensitivity is 0.44 A/W. When  $I_p$  was measured, the 0.83- $\mu\text{m}$  wavelength laser beam was led to the MSM-PD through a 50- $\mu\text{m}$  diameter optical fiber. This beam did not cover the entire light-sensitive area. The capacitance of a sealed MSM-PD was determined to be 0.2 pF and is independent of external bias. The measured capacitance includes the capacitance of the case. The actual capacitance of the MSM-PD is less than 0.2 pF. This MSM-PD is a high-speed device.

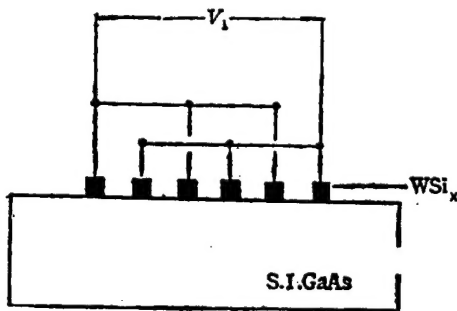


Figure 1. The MSM-PD Structure

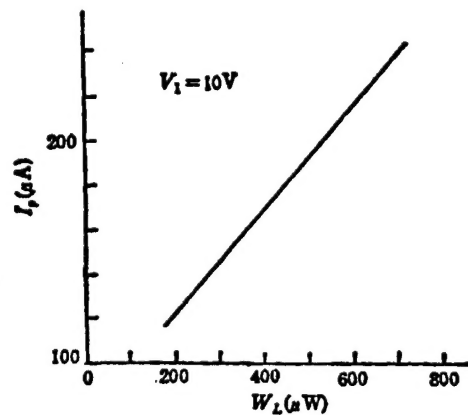


Figure 2. Photocurrent  $I_p$  vs. Input Light Power  $W_L$  of the MSM-PD

## II. Realization of Monolithic Integration

Based on the above discussion, the MSM-PD is a simple and easy-to-make detector. We used semi-insulating GaAs as the substrate and formed the MESFET channels by ion implantation with Si. The gate electrodes are made of WSi<sub>x</sub> in the amplifier. Thus, the MSM-PD can be fabricated in the same semi-insulating GaAs surface. The reaction between the structure of the MSM-PD and that of the

MESFET is shown in Figure 3. There are two primary techniques in monolithic integration: mesa structure and planar structure. With regard to the former, the process mainly involves the following steps: 1) Prepare the semi-insulating GaAs surface; 2) implant Si ions into the GaAs surface; 3) anneal the GaAs, which is covered with an Si wafer, under non-steady-state condition in a diffusion furnace under  $N_2$  atmosphere at  $750\sim 900^\circ C$  for 1~2 minutes; 4) etch out the MESFET mesa to electrically insulate the MESFET region; 5) use sputtering and RIE [reactive ion etching] to etch out  $WSi_x$  to form the MSM-PD electrodes and the MESFET gate electrodes; and 6) prepare the ohmic contacts and connecting lines for the MESFET. The planar structure uses somewhat different techniques. After surface preparation is made, a layer of  $AlN_x$  is sputtered on it. Then, the  $AlN_x$  film in the MESFET region is etched away and Si ions are selectively implanted into it. Before sputtering  $WSi_x$ , the  $AlN_x$  film in the MSM-PD region is etched away to expose the semi-insulating GaAs surface. Then,  $WSi_x$  sputtering and etching follow. Because of selective ion implantation, electrical insulation is naturally created between the MESFET's. In the planar structure, self-aligned ion implantation may be used to improve the performance of the MESFET. However, some adjustment may be necessary.

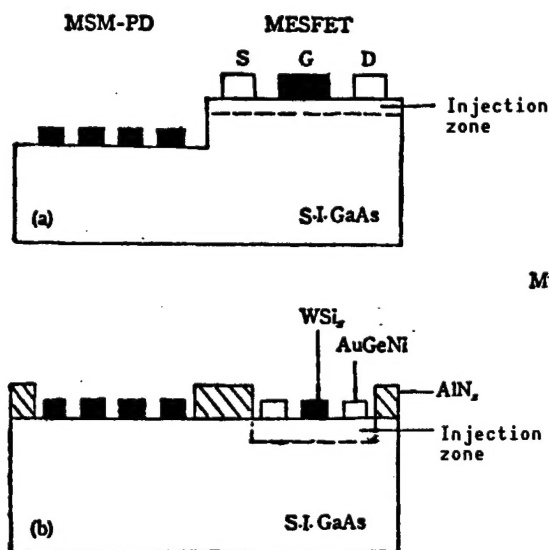


Figure 3. Structure of MSM-PD and MESFET  
(a) Mesa structure;  
(b) Planar structure

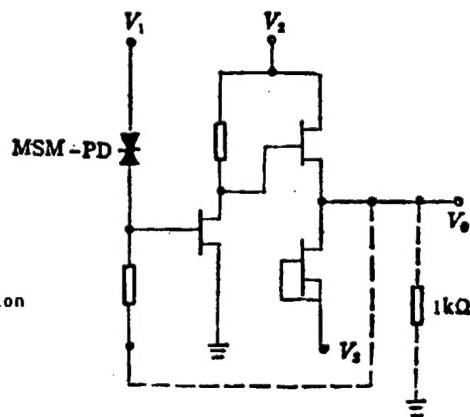


Figure 4. Monolithically Integrated Electrical Circuit  
(Dotted line indicates external connection)

Figure 4 shows the circuit diagram for the monolithic integration. It is composed of a detector, an amplifier, and a follower. The MSM-PD electrode is still  $4\ \mu m$  wide and the spacing is still  $4\ \mu m$  apart. The light-sensitive area is  $100\ \mu m \times 100\ \mu m$ . For the MESFET,  $L_g$  (gate length) =  $4\ \mu m$  and  $W_g$  (gate width) =  $120\ \mu m$  and the source-drain spacing  $L_{os}$  =  $12\ \mu m$ . Figure 5 shows the curve for output voltage  $V_o$  versus input light power  $W_L$ . The figure also shows the bias conditions during the time of measurement. From the  $V_o$  vs.  $W_L$  curve, the voltage sensitivity of the circuit is  $40\ mV/100\ \mu W$ . During the time of measurement



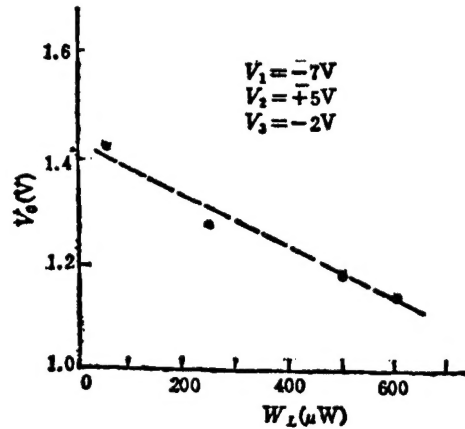


Figure 5. Output Voltage  $V_0$  vs.  $W_L$

a 1 k $\Omega$  resistor was put across the output. In actual applications, we cannot have such a large resistance, which would affect the speed of the device. Figure 6 [photograph not reproduced] shows the electrical response to the input light signal detected by the monolithically integrated chip. An optical signal is converted to an electrical signal. In this measurement, a modulated power supply was used to power a GaAlAs/GaAs laser. The modulated laser beam was led to the MSM-PD through a 50- $\mu m$  diameter optical fiber. The electrical resonance was obtained from the output of the circuit. In Figure 6, the laser beam was regulated by modulating the current flowing through the laser. Due to certain limitations, it is not possible to perform high-speed measurement with the circuit.

### III. Conclusions

Based on the fact that it is simple and easy to fabricate on MSM-PD on GaAs and it is compatible with the GaAs MESFET technology, monolithic integration of a short-wavelength detector and amplifier on GaAs becomes an easy task. This point has been proven in our work. This monolithic integrated circuit has been developed in two different structures. Some preliminary characteristics have been determined. Next, we plan to modify the technology to improve the performance of the circuit and to measure its high-speed characteristics. The authors wish to take this opportunity to thank the people on the fabrication line in the Institute of Semiconductors' 7th Laboratory and Cheng Meiqiao [4453 5019 0829] and Zhou Fan [0719 1581] of the Common Technology Research Laboratory for their support and assistance.

### References

1. T. Sugeta, et al., JPN. J. APPL. PHYS., Vol 19, 1980, p 459.
2. M. Ito, et al., IEEE ELECTRON DEVICE LETTERS, EDL-5, 1984, p 531.

- END -